MODELING SNOW CRYSTAL GROWTH III:
three-dimensional snowfakes

Janko Gravner
Mathematics Department
University of California
Davis, CA 95616
e-mail: gravner@math.ucdavis.edu

David Griffeath
Department of Mathematics
University of Wisconsin
Madison, WI 53706
e-mail: griffeat@math.wisc.edu

(Preliminary version, April 2007)

Abstract We introduce a three-dimensional, computationally feasible, mesoscopic model for snow crystal growth, based on diffusion of vapor, anisotropic attachment, and a semi-liquid boundary layer. Several case studies are presented that faithfully emulate a wide variety of physical snowflakes.

2000 *Mathematics Subject Classification*. Primary 82C24. Secondary 35R35, 60K35.

Keywords: Coupled lattice map, crystal growth, diffusion-limited aggregation, Stefan problem.

Acknowledgments. We extend our continuing appreciation and gratitude to Ken Libbrecht for sharing with us his unmatched collection of snowflake photographs and his extensive research on snowflake physics. We also thank Antoine Clappier for introducing us to ray-tracing.

Support. JG was partially supported by NSF grant DMS–0204376 and the Republic of Slovenia's Ministry of Science program P1–285. DG was partially supported by NSF grant DMS–0204018.

1 Introduction

In this paper we exhibit some virtual snowflakes, or *snowfakes*, generated by a natural, fully three-dimensional algorithm for snow crystal evolution. The present study extends our earlier work on growth and deposition [**GG1**, **GG2**, **GG3**], and other previous efforts in this direction [**Pac**, **Rei**]. The key features of our model are *diffusion* of vapor, anisotropic *attachment* of water molecules, and a narrow *semi-liquid layer* at the boundary. All three ingredients seems to be essential for faithful emulation of the morphology observed in nature.

Growth of a snow crystal in a homogeneous environment, that is, in constant weather conditions, is primarily dependent on temperature, pressure and vapor density. However, the principles by which these determine how supersaturated vapor attaches to a growing ice crystal are poorly understood [**Lib4**]. Therefore, incorporating this process into a mathematical model in terms of tunable parameters is a sensible strategy. While it is not a priori clear how our parameters correlate with physical conditions, experimentation provides valuable clues (cf. Sections 7–13). This approach also makes it possible to model inhomogeneous environments by varying the parameters during the evolution (cf. Section 12). As a reasonable first step, the diffusion of latent heat, generated by solidification [**Lib4**], is neglected, as are surface diffusion [**Lib4**], impedance [**NB**] and other effects that may be important in some regimes. Based on the verisimilitude between snowfakes and actual snow crystals (the most convenient resource for such comparison is Libbrecht's field guide [**Lib6**]), it would appear that this approach is able to shed light on a substantial portion of snow crystal physics.

The algorithm assumes a mesoscopic (micron) scale of basic units for the ice crystal and water vapor, which eliminates inherent randomness in the diffusion and the attachment mechanism. This brings the process within reach of realistic simulation; by contrast, any three-dimensional approach based on microscopic dynamics is completely beyond the scope of present computing technology. We refer the reader to [**GG3**] for a brief history of snow crystal observation and modeling, background on our approach in a two-dimensional setting, and many references to the literature. See also [**NR**] for another attempt at spatial mesoscopic modeling.

There are many papers and books, for a variety of audiences, dealing with snowflake photography and classification, the underlying physics, or some combination thereof, so we will not offer a comprehensive review here. Excellent introductions to the subject include *the* classic book by Nakaya [**Nak**], early empirical studies and classification schemes [**BH**] and [**ML**], and more recent papers and books by K. Libbrecht [**Lib1**, **Lib2**, **Lib3**, **Lib4**, **Lib5**, **LR**]. Among research papers that attempt to decipher the three-dimensional aspects of snow crystals, the standout reference is [**TEWF**]; also worth mentioning are [**Iwa**], [**NK**] and [**Nel**].

As a preview of the capabilities of our model, let us illustrate the crystal tip instability and initiation of side branching studied in the laboratory by Gonda and Nakahara [**GN**]. A sequence of four still frames from their paper was reproduced in [**GG3**] so we will not show it here. But Fig. 1 depicts the top view of a corresponding snowfake at four different times (12, 15, 18, and 21 thousand), and oblique views of the crystal's top and bottom at the final time. The parameters are: $\beta_{01} = 2.8$, $\beta_{10} = \beta_{20} = 2.2$, $\beta_{11} = \beta_{21} = 1.6$, $\beta_{30} = \beta_{31} = 1$, $\kappa \equiv .005$, $\mu_{10} = \mu_{20} = .001$, $\mu = .0001$ otherwise, $\phi = .01$, and $\rho = .12$. Their role, and that of the initial state, will be described in Section 2. Similarity between the real and simulated sequences is striking: in both instances a defect arises at a characteristic distance from the crystal tip, becomes more

pronounced, and later gives rise to a side branch with its own ridge structure similar to that of the main branch. Note also that our snowfake has its ridges, and most other markings, on the top side; the bottom is almost featureless. This is due to a small downward drift in our model, an aspect we will discuss later in more detail. The direction of the drift represents the motion of the crystal in the opposite direction — we prefer upward motion because interesting features then appear on top, although this would obviously correspond to the bottom of a falling snowflake. We should also note that the drift value means that, during its evolution, our simulated crystal moved for about 200 space units, which is comparable to the diameter it reached. This is typical of drift values that erase features on one side without otherwise significantly changing the morphology. Our model thus predicts that a significantly larger range of motion during growth is not possible for most interesting physical snow crystals, such as dendrites or plates. Another example of our algorithm's potential to make new predictions about basic aspects of snow crystal growth is the location of markings. From micrographs, it is almost impossible to tell whether these are on the top, bottom, or inside a given physical specimen, so little attention has been paid to this issue to date. We have gathered a considerable amount of evidence that inside markings are quite common (cf. Sections 7, 8 and 9).

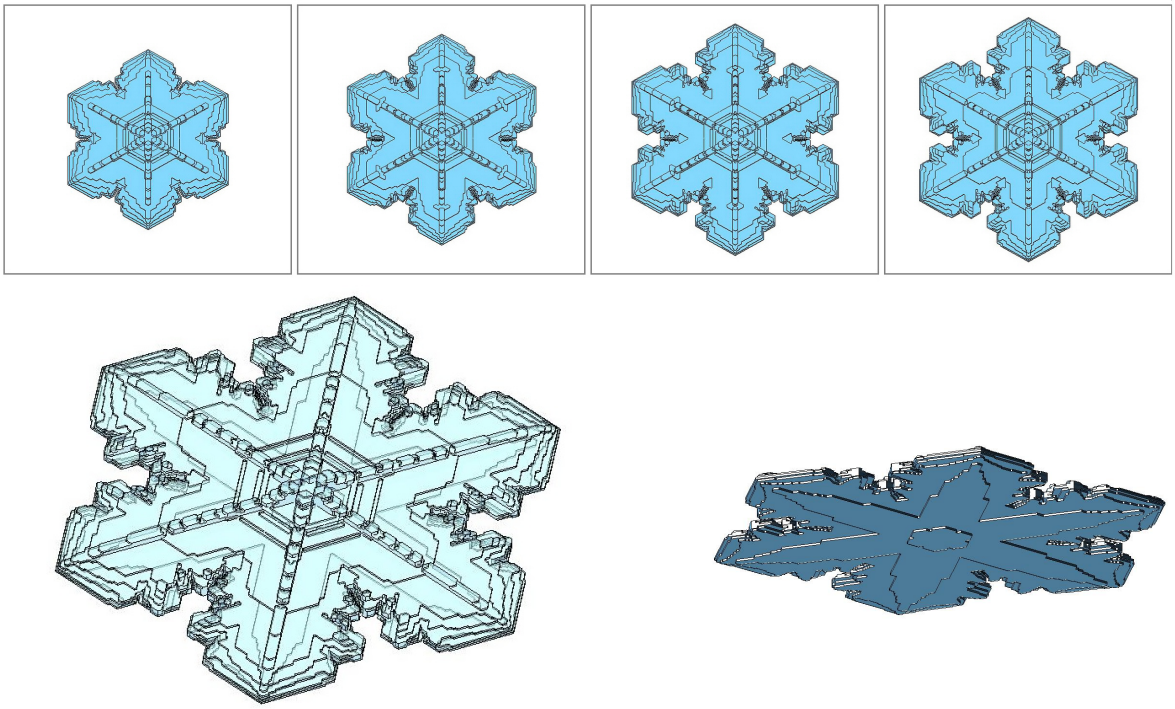

Fig. 1. Tip instability and oblique top (*left*) and bottom (*right*) views of the final crystal.

Our account will focus on seven case studies that reproduce many features commonly observed in actual snowflakes: ridges, ribs, flumes and other "hieroglyphs," formation of side branches, emergence of sandwich plates, hollow columns, hollow prism facets, and so forth. We also explore dependence on the density of vapor, and the aforementioned effect of drift, and inhibition of side branches by the semi-liquid layer. Varying meteorological conditions during growth are considered very important [**Lib6**] so we include several examples, such as plates with dendritic tips and capped columns, that are believed to arise due to sudden changes in the weather. However, we will encounter snowfakes that grew in a homogeneous environment

but give the impression that they did not. We will occasionally address dependence of the final crystal on its early development, and conclude with a few eccentric examples that may be too brittle to occur in nature. These typically arise near a phase boundary, when the dominant direction of growth is precarious. A complete collection of snowfakes from our case studies (with some additional information, such as simulation array sizes), a collection of movies, and a slide show are available for download from:

`http://psoup.math.wisc.edu/Snowfakes.htm`

The first order of business, in the next section, is to describe the snowfake algorithm in detail. Four subsequent sections discuss computer implementation and visualization tools, mathematical foundations, parameter tuning, and extensions of the model. The remainder of the paper is then devoted to the case studies.

2 The algorithm for three-dimensional snow crystal growth

Our basic assumptions are as follows:

A1. The mesoscopic (micron-scale) building blocks are (appropriately scaled) translates of the *fundamental prism*, which has hexagonal base of side length $1/\sqrt{3}$ and height 1;

A2. In its early stages of growth, from microscopic to mesoscopic, the crystal forms a hexagonal prism, and then it maintains this shape until it reaches the size of a few microns across.

A3. Diffusion outside the crystal is isotropic except possibly for a small drift in the vertical direction;

A4. Crystallization rates depend on the direction and local convexity at the boundary;

A5. Melting at the boundary creates a semi-liquid layer.

Note that the side (rectangular) faces of the fundamental prism are commonly referred to as *prism* faces, while the top and bottom (hexagonal) ones are called *basal* faces.

The lattice for our model is $\mathbb{T} \times \mathbb{Z}$, where $\mathbb{T}$ is the planar triangular lattice (see Fig. 2). This is not precisely the crystalline lattice of hexagonal ice *Ih*, which is obtained by removing certain edges and sites from $\mathbb{T} \times \mathbb{Z}$, and then applying a periodic deformation [**NR**], but we are constructing a mesoscopic model that should obscure such fine details. Therefore, each $x \in \mathbb{T} \times \mathbb{Z}$ has 8 neighbors, 6 in the $\mathbb{T}$-direction and 2 in the $\mathbb{Z}$-direction.

At each discrete time $t = 0, 1, 2, \ldots$, $A_t \subset \mathbb{T} \times \mathbb{Z}$ represents the snowfake, and with each site $x \in \mathbb{T} \times \mathbb{Z}$ we associate two varieties of mass:

$b_t(x) =$ the *boundary mass* at x at time t (*frozen* if $a_t(x) = 1$, *semi-liquid* if $a_t(x) = 0$),
$d_t(x) =$ the *diffusive mass* at x at time t (*vapor*).

The state of the system at time t at site x is therefore $(a_t(x), b_t(x), d_t(x))$, where a_t is the attachment flag

$$a_t(x) = \begin{cases} 1 & \text{if } x \in A_t, \\ 0 & \text{otherwise.} \end{cases}$$

Our dynamics assumes that the diffusive and the semi-liquid mass both change to ice when the site joins the crystal, and stay in that state thereafter. The two types of mass can coexist on the boundary of the snowfake, but only boundary mass persists inside the snowfake while only diffusive mass occurs outside and away from the boundary.

The initial state will consist of frozen mass 1 at each site of some finite set, on which also $a_0 \equiv 1$, with a_0 and $b_0 \equiv 0$ and $d_0 \equiv \rho$ everywhere else. In keeping with assumption (A2), the most natural choice for this finite set, a singleton at the origin, often does not work well, as its $\mathbb{Z}$-direction neighbors see 7 neighbors off the crystal's boundary. This means that it is common, even for low ρ, that the dynamics immediately triggers a rapid expansion in the $\mathbb{Z}$-direction. To prevent this singularity, our canonical initial state consists of a hexagon of radius 2 and thickness 1, consisting of 20 sites. Other non-symmetric initial states will be discussed later.

Let us now describe the update rule of our snowflake simulator, which performs steps (i)–(iv) below in order every discrete time unit. The reader should observe that total mass is conserved by each step, and hence by the dynamics as a whole.

Write $\mathcal{N}_x^{\mathbb{T}} = \{x\} \cup \{y : y \text{ is a neighbor of } x \text{ in the } \mathbb{T}\text{-direction}\}$, $\mathcal{N}_x^{\mathbb{Z}} = \{x\} \cup \{y : y \text{ is a neighbor of } x \text{ in the } \mathbb{Z}\text{-direction}\}$ for the $\mathbb{T}$-*neighborhood* and $\mathbb{Z}$-*neighborhood* of x, respectively. We also let $\mathcal{N}_x = \mathcal{N}_x^{\mathbb{T}} \cup \mathcal{N}_x^{\mathbb{Z}}$, and set the the (outside) boundary of the snowfake at time t to be $\partial A_t = \{x \notin A_t : y \in A_t \text{ for some } y \in \mathcal{N}_x\}$ and $\bar{A}_t = A_t \cup \partial A_t$.

The complement of a set A is denoted by A^c. Also, we use $^\circ$ (degree) and $'$ (prime) notation to denote amounts of mass before and after a step or substep is completed. If there is more than one intermediate step, we use double primes. This is necessary since some mass allocations may change more than once during a single cycle of the steps. At the end of each cycle the time t advances to $t + 1$.

Steps of the update rule:

i. Diffusion

Diffusive mass evolves on A_t^c in two, or possibly three, substeps. The first substep is by discrete diffusion with uniform weight $\frac{1}{7}$ on the center site and each of its $\mathbb{T}$-neighbors. Reflecting boundary conditions are used at the edge of the crystal. In other words, for $x \in \bar{A}_t^c$,

$$d_t'(x) = \frac{1}{7} \sum_{y \in \mathcal{N}_x^{\mathbb{T}}} d_t^\circ(y). \tag{1a}$$

The second substep does the same in the $\mathbb{Z}$-direction:

$$d_t''(x) = \frac{4}{7} d_t'(x) + \frac{3}{14} \sum_{y \in \mathcal{N}_x^{\mathbb{Z}}, y \neq x} d_t'(y). \tag{1b}$$

For $x \in \partial A_t$ any term in the sum in (1a) (resp. (1b)) corresponding to $y \in A_t$ is replaced by $d_t^\circ(x)$ (resp, $d_t'(x)$).

The reason for the weights in (1b) is as follows. Imagine we tessellate $\mathbb{R}^3$ with translates of the fundamental prism and scale the lattice $\mathbb{T} \times \mathbb{Z}$ so that the lattice points are in the centers of these prisms. The "bonds" in the top left frame of Fig. 2 thus all have unit length and we eventually visualize the crystal by drawing prisms that are centered about sites of A_t. Rule (1b) ensure that diffusion on the scaled lattice is isotropic, in agreement with assumption A2.

As mentioned in the Introduction, there is also good reason to consider the more general case of diffusion with drift in the $\mathbb{Z}$-direction, corresponding to downward (or upward) motion of the snowflake. The third diffusion substep is thus:

$$d_t'''(x) = (1 - \phi \cdot (1 - a_t(x - e_3)) \cdot d_t''(x) + \phi \cdot (1 - a_t(x + e_3)) \cdot d_t''(x + e_3), \tag{1c}$$

where $e_3 = (0, 0, 1)$ is the third basis vector. Parameter ϕ measures the strength of the drift, and needs to be small for the dynamics to remain diffusion-limited.

ii. Freezing

Assume that $x \in \partial A_t$, and denote

$$n_t^{\mathbb{T}}(x) = \#\{y \in \mathcal{N}_x^{\mathbb{T}} : a_t^\circ(y) = 1\} \wedge 3, \quad n_t^{\mathbb{Z}}(x) = \#\{y \in \mathcal{N}_x^{\mathbb{Z}} : a_t^\circ(y) = 1\} \wedge 1. \tag{2a}$$

Proportion $1 - \kappa(n_t^{\mathbb{T}}(x), n_t^{\mathbb{Z}}(x))$ of the diffusive mass at x becomes boundary mass. That is,

$$\begin{aligned} b_t'(x) &= b_t^\circ(x) + (1 - \kappa(n_t^{\mathbb{T}}(x), n_t^{\mathbb{Z}}(x)))d_t^\circ(x), \\ d_t'(x) &= \kappa(n_t^{\mathbb{T}}(x), n_t^{\mathbb{Z}}(x))d_t^\circ(x). \end{aligned} \tag{2b}$$

The seven parameters $\kappa(i, j)$, $i \in \{0, 1\}$, $j \in \{0, 1, 2, 3\}$, $i+j > 0$, constitute one of the ingredients that emulate the dynamics of the semi-liquid layer at the boundary of the crystal. The other ingredient, μ, appears in step *iv* below. We assume that κ decreases in each coordinate since "more concave corners" at the boundary ∂A_t, i.e., those with more neighbors in A_t, should catch diffusing particles more easily.

iii. Attachment

Assume again that $x \in \partial A_t$ and define the neighborhood counts as in (2a). Then x needs boundary mass at least $\beta(n_t^{\mathbb{T}}(x), n_t^{\mathbb{Z}}(x))$ to join the crystal:

$$\text{If } b_t^\circ(x) \geq \beta(n_t^{\mathbb{T}}(x), n_t^{\mathbb{Z}}(x)), \text{ then } a_t'(x) = 1. \tag{3}$$

Again, we have seven parameters $\beta(i, j)$, $i \in \{0, 1\}$, $j \in \{0, 1, 2, 3\}$, $i+j > 0$, and the assignment only makes physical sense if β decreases in each coordinate.

In addition, we assume that $a_t'(x) = 1$ automatically whenever $n_t^{\mathbb{T}}(x) \geq 4$ and $n_t^{\mathbb{Z}}(x) \geq 1$. This last rule fills holes and makes the surface of the crystal smoother, without altering essential features of the dynamics.

At sites x for which $a_t'(x) = 1$, the diffusive mass becomes boundary mass: $b_t'(x) = b_t^\circ(x) + d_t^\circ(x)$, $d_t'(x) = 0$. Attachment is permanent, and there are no further dynamics at attached sites. Thus we do not model sublimation, although it may play a significant role in the last stages of snow crystal evolution (cf. p. 27 of [**Lib6**]).

iv. Melting

Proportion $\mu(n_t^{\mathbb{T}}(x), n_t^{\mathbb{Z}}(x))$ of the boundary mass at each boundary site becomes diffusive mass. Thus, for $x \in \partial A_t$,

$$\begin{aligned} b_t'(x) &= (1 - \mu(n_t^{\mathbb{T}}(x), n_t^{\mathbb{Z}}(x)))b_t^\circ(x), \\ d_t'(x) &= d_t^\circ(x) + \mu(n_t^{\mathbb{T}}(x), n_t^{\mathbb{Z}}(x))b_t^\circ(x). \end{aligned} \tag{4}$$

Again, μ is decreasing in each coordinate.

Fig. 2 summarizes our model in three frames. At the upper left is a portion of the underlying lattice $\mathbb{T} \times \mathbb{Z}$. The central site represented as a larger black ball has its neighborhood indicated in black, and a translate of the fundamental prism is centered at that site. In the upper right detail, blue translates of the fundamental prism are drawn around each site of a small crystal. Seven boundary sites are depicted in red and each is labeled by its boundary configuration. For example, the "21" site has 2 horizontal ($\mathbb{T}$-) neighbors and 1 vertical ($\mathbb{Z}$-) neighbor, and consequently needs boundary mass β_{21} to join the crystal. Finally, the lower panel shows a flowchart for the algorithm. There are three epochs in the life of a site. Away from the crystal's boundary, it only exchanges diffusive mass d_t with its neighbors. Once the crystal grows to reach the site's neighborhood, two additional effects, melting and freezing, promote exchange between diffusive mass d_t and boundary mass b_t. Final changes occur once boundary mass exceeds the threshold β (which depends on the neighborhood configuration): the site attaches and the two types of mass merge into b_t.

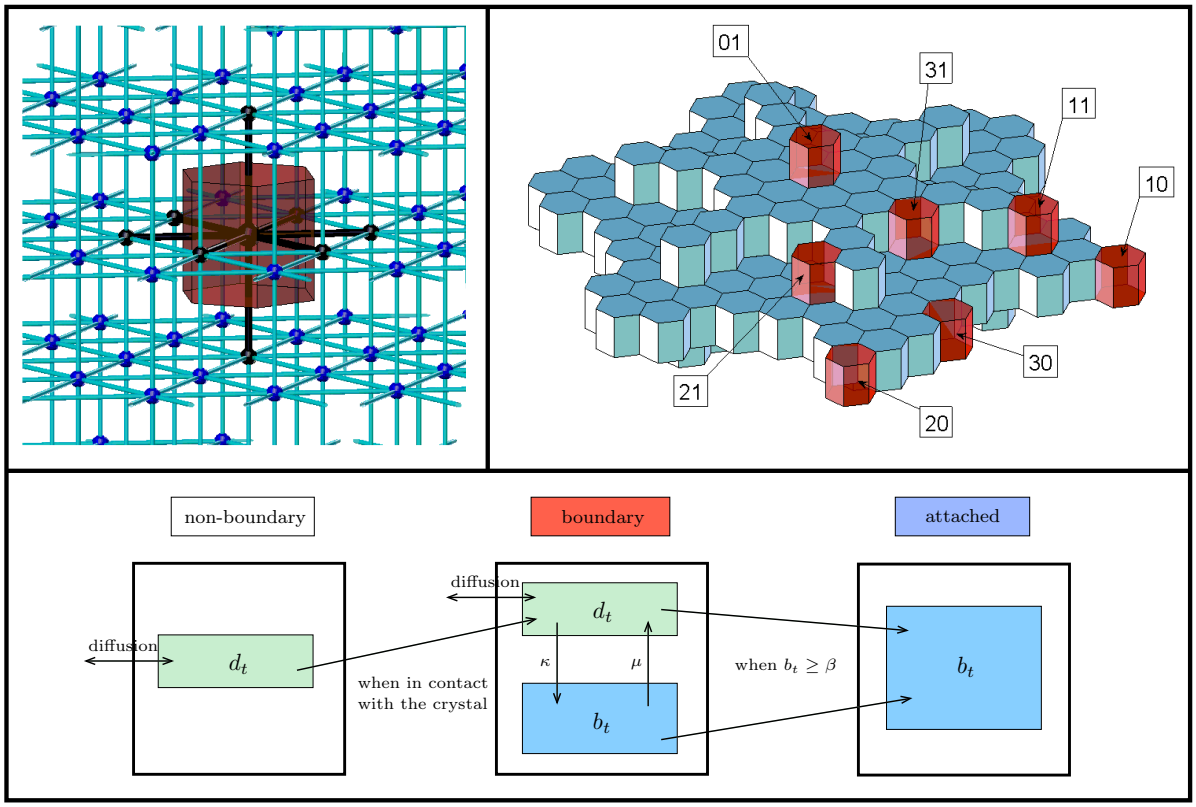

Fig. 2. The stacked triangular lattice $\mathbb{T} \times \mathbb{Z}$ (*top left*), coding of boundary configurations (*top right*), and a flowchart for the growth algorithm (*bottom*).

3 Notes on computation and visualization

Following the same strategy as for our previous two-dimensional model [**GG3**], the dynamics actually run on the cubic lattice $\mathbb{Z}^3$, which can be mapped onto $\mathbb{T}^2 \times \mathbb{Z}$. Our basic computational engine is written in C, but MATLAB is used for mapping and visualization. As mentioned previously, the snowfakes are depicted by drawing visible boundaries of translates of the fundamental prism centered on sites of A_t. Since this straightforward procedure makes jagged vertical boundaries, we apply a smoothing algorithm at the boundary that enlarges the crystal by no more than one mesoscopic unit. (This algorithm has *no* effect the dynamics and is *not* applied to the small snowfake in Fig. 2.) MATLAB's `patch` routine renders the faces. For better results we then emphasize edges using the `line` routine.

MATLAB's visualization tools certainly provide adequate representations for detailed investigation of the resulting crystals. They do not, however, give a satisfactory comparison with the best snowflake photographs [**LR**, **Lib5**, **Lib6**], typically taken from directly above the (predominantly two-dimensional) crystal, which is in turn illuminated from below. This viewpoint can be effectively simulated by ray-tracing, as implemented here by the POV-Ray software [**POV**]. Our program automatically outputs a file with a triangulation of the crystal's boundary, which is then used by the `mesh2` command in POV-Ray.

We would like to point out that both the algorithm and visualization procedures require considerable computing power and memory. At present (fall 2007), our simulations are very time consuming, barely feasible on commercial personal computers. (In fact, an adaptive resolution algorithm is necessary to make the boundary descriptions manageable.) Progress in studying snowfakes is therefore quite slow, precluding systematic classification of the dynamics. Our goal has been to find representative examples that seem to replicate physical snow crystals and thereby shed light on their evolution.

When there is no drift ($\phi = 0$), the initial state is a hexagonal prism, and the space is a finite lattice in the shape of hexagonal prism with appropriate periodic boundary conditions, symmetry can be exploited for computational efficiency. In fact, in this case it suffices to compute the dynamics on $\frac{1}{24}$ of the whole space. However, there are two good reasons for giving up complete symmetry of the rule. First, the initial state may not be symmetric, and second, the diffusion may have a drift. For computations to still proceed at a reasonable speed, we only give up reflectional symmetry around the xy-plane (recall that the drift is only in the $\mathbb{Z}$-direction), allowing the initial state to depend on the z coordinate, but retaining its hexagonal symmetry in the x and y coordinates. This increases the space and time demands of the fully symmetric program by a factor of 2.

The program stops automatically when the density at the edge of the lattice falls below a given proportion of the initial density (typically $2\rho/3$ or $\rho/2$), or when the crystal gets too close to the edge (snowfake radius greater than 80% the radius of the system).

4 Connection to pde, and size of the parameter space

For simplicity, we assume that $\phi = 0$ until the last paragraph of this section. Mathematically, our algorithm is a discrete space and time version of a *free boundary*, or *Stefan*, problem [**Lib2**, **Lib3**, **Lib4**]. This is a partial differential equation (pde) in which the crystal is represented by a growing set A_t and the density (i.e., supersaturation) of vapor outside it as $u = u(x, t)$. Then u is 0 on the boundary ∂A_t, and satisfies the diffusion equation outside the crystal

$$\frac{\partial u}{\partial t} = \Delta u, \quad x \in A_t^c. \tag{1.1}$$

The velocity of the boundary at a point $x \in \partial A_t$ with outside normal ν is given by a function

$$w\left(\frac{\partial \rho}{\partial \nu}, \nu\right). \tag{1.2}$$

Considering the slow growth of A_t, diffusion equation (1.1) may be simplified to its equilibrium counterpart $\Delta u = 0$ [**Lib2**, **Lib3**, **Lib4**], which makes this into an anisotropic version of the *Hele-Shaw* problem.

Presumably under diffusion scaling, in which space is scaled by ϵ, time by ϵ^{-2}, and $\epsilon \to 0$, the density field and the occupied set in our model converge to a solution of the Stefan problem. However, a rigorous justification for this connection, and identification of the limit w in terms of model parameters, at present remain elusive.

The boundary velocity function $w = w(\lambda, \nu) \geq 0$ is defined for $\lambda \geq 0$ and three-dimensional unit vectors $\nu \in S^2$. In order to develop a rigorous mathematical theory, the most convenient assumptions are that w is continuous in both variables, nondecreasing in λ, and satisfies $w(\lambda, \nu) \leq C\lambda$ for some constant C independent of λ and ν. Under these conditions, the non-isotropic *melting* version of the Stefan problem (1.1–1.2), which has w replaced by $-w$ in (1.2), has a unique viscosity solution at all times $t \geq 0$, starting from any smooth initial crystal. This is proved in [**Kim**] for the isotropic case (when w is constant); assuming the listed properties of w, the proof extends to our general setting. On the other hand, the *freezing* version (1.1–1.2) considered here presents a much greater challenge. It has long been known that the crystal's boundary will not remain smooth [**SB**], and no general theory of existence and uniqueness of generalized solutions is developed. The inherent difficulties will be no mystery once we present our simulations, which feature a considerable variety of singularities and instabilities. These may make direct numerical computation with the pde questionable, explaining why numerical pde-based models for snow crystal growth have not been satisfactory (cf. [**Sch**]). For further mathematical theory and references, we refer the reader to [**Kim**, **CK**].

For the sake of further discussion in this section, we posit that our scheme approximates an appropriate generalized solution, presumably of viscosity type, of (1.1–1.2), and thus that the macroscopic evolution of the crystal is uniquely determined by its initial state and the velocity function w.

For the model introduced in Section 2, $w(\lambda, u)$ will be linear in λ, since the attachment and melting rates are independent of the vapor density. This may not always be the case; in fact, some of the literature even considers the possibility that w is non-monotone in λ [**Lib3**, **GG3**]. Analysis of such cases would present new theoretical challenges, and from simulations of our 3d model it appears that nonmonotonicity is not needed for observed phenomena in nature. Monotone nonlinearity, arising from monotone density dependent rates, is harder to dismiss and worth further investigation – for instance, it is possible that w vanishes for very small λ.

The function w is determined by very few physical parameters, perhaps just two: temperature and atmospheric pressure [**Lib2**, **Lib3**, **Lib4**]. Therefore, possible evolutions from a fixed seed comprise a three-dimensional manifold (its coordinates being the supersaturation level, temperature, and pressure) in an infinite-dimensional space of possible velocities w. Much of the ongoing snow crystal research constitutes an attempt to understand the structure of this manifold, a daunting task since the underlying (perhaps quantum) attachment physics is very poorly understood, controlled homogeneous environments are hard to design, and crystal evolution is difficult to record. Our model does not have these problems. Instead, its main weakness is the number of free parameters that need to be tuned to approximate w at a particular temperature and pressure. It helps that our parameters have intuitive meaning, but finding a particular realistic snowfake involves approximating an a priori infinite-dimensional object w by one of finite but high dimensionality. The challenge is compounded by very incomplete information – all that is typically observable in nature is the final crystal, which may have been subjected to numerous changes in conditions and orientation during growth, as well as sublimation and perhaps even artifacts of the recording process. It is thus no surprise that our parameter selection is an arduous and imprecise task.

In the next section we will describe some ad hoc rules that we have used to generate our case studies, but the issue of parameter selection is in dire need of further investigation. What we can say is that the best examples are quite sensitive to perturbations in w. Thus they require good approximations and a large number of judicious parameter choices. In addition, the dependence on the initial seed is often quite dramatic. These observations underscore both the marvel and the fragility of natural snowflakes.

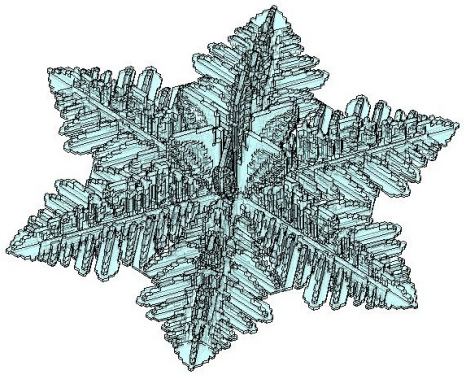

Fig. 3. A "failed" snowfake.

At the same time, we wish to emphasize the conceptual simplicity of our model. The large parameter space is a consequence of geometry rather than an excessive number of modeling ingredients. Apart from the two scalar parameters – density ρ and drift ϕ – we have only three vector parameters — attachment threshold β, freezing rate $1-\kappa$, and melting rate μ — whose high dimensionality arises from the many possible boundary arrangements. The parameter set can be reduced, but *some* tuning will always be necessary, as illustrated by the "random" crystal in Fig. 3. This was obtained by choosing $\kappa \equiv .1$, $\mu \equiv .001$, $\rho = .1$, $\phi = 0$, and all β's equal to 1 except $\beta_{01} = 1.73$ and $\beta_{10} = \beta_{20} = 1.34$. These values are in a sensible neighborhood of the parameter space, but the last two attachment rates were selected by chance. The result has some physically reasonable features, but one immediately notices an excessive density of branches and inordinately high ridges. In general, visual comparison with snow crystal photographs is the only method we use to decide whether a snowfake is a "failure" or a "success."

5 Effective choice of parameters for simulations

While realistic choices of parameters require considerable guesswork, there are a few guidelines we have developed. Some come from mathematical arguments, others from experimentation; both are described in this section.

We typically choose the drift parameter ϕ last, and on the order of .01. This keeps $\phi \approx 1/(\text{array size})$, as required for a diffusion limit, and produces essentially one-sided markings. The rest of this section is devoted to other parameters and assumes $\phi = 0$.

Our simulator represents diffusion by discrete averaging in time t, which is also discrete. The bulk effects of this operation expand at the rate $\sqrt{t}$, although the extreme radius of its influence, which is known as the *light cone* in cellular automata research, grows linearly in t. If the initial density ρ of our discrete vapor field is too large, then the crystal may expand in some direction as fast as the light cone, or perhaps fall behind it by $\mathcal{O}(\sqrt{t})$. We call parameter sets leading to this behavior the *Packard regime*; it is clearly not physical, as it depends on the discrete nature of the averaging. However, systems of this sort are able to generate fractal plates reminiscent of Packard snowflakes [**Pac**, **GG3**] and exhibit one variety of faceting (cf. [**NR**]). In our simulations we systematically avoid the Packard regime by keeping the density low. For the extremal points of our snowfakes not to expand as fast as the light cone, the conditions are

$$(1-\kappa_{01})\rho < \beta_{01}, \quad (1-\kappa_{10})\rho < \beta_{10},$$

as is easy to see from the description of the rule. Our densities are typically considerably smaller, since large densities generate expansion that is too rapid to be realistic, at least in its initial stages. As mentioned previously, a surprisingly important role is also played by the choice of initial seed.

On the other hand, it is clear that a very large melting rate will stop growth altogether. This happens if the flow out of the boundary mass exceeds the flow in just before that mass exceeds the threshold for attachment. A sufficient condition for continual growth in all directions is therefore

$$\mu_{01}\beta_{01} < (1-\kappa_{01})\rho, \quad \mu_{10}\beta_{10} < (1-\kappa_{10})\rho,$$

since the 01 and 10 boundary arrangements always have the slowest potential growth. In the great majority of examples we will present, parameters for the 20 and 10 arrangements agree.

In this case, the last condition is necessary as well — if it does not hold, then the growth is convex-confined in the $\mathbb{T}$-direction.

Let us now describe a few rules of thumb when searching for snowfakes that emulate nature. We commonly start with a *reduced* parameter set. Namely, we set the κ's to a common value, say, $\kappa \equiv .1$. Then we select two different β parameters, β_{01} and $\beta_{10} = \beta_{20} = \beta_{11}$, with all the remaining β's fixed to 1. The size of β_{20} controls the strength of the convexifying mechanism, assumed to be the same in both the xy and z directions. Indeed, if β_{20} is large, then the crystal will remain a perfect hexagonal prism for a long time. The only other parameters are the common value of all μ's and the vapor density ρ. This is a more manageable four-parameter space that encodes four essential elements of three-dimensional snowflake growth, each with a single tunable parameter: diffusing supersaturation level (ρ), convexifying strength (β_{20}), semi-liquid layer smoothing (μ), and preference for the $\mathbb{Z}$-direction over the $\mathbb{T}$-direction (β_{01}/β_{20}). This scheme is used to identify the neighborhood of a desired morphological type in phase space. Then parameters are perturbed for added realism.

One of the most important lessons of our two-dimensional model [**GG3**] was that the melting parameter μ inhibits side-branching and is therefore important for dendrite formation. When $\mu \equiv 0$, it seems impossible to avoid an excessive density of branches. Indeed, this role of μ is easily understood. Namely, μ creates a positive density at the boundary, due to flow out of the boundary layer. This density has the effect of reducing the ambient vapor density by a fixed amount, independent of location, and hence disproportionately affects regions of smaller density. (To a very rough first approximation [**Lib4**], the expansion speed is proportional to $\sqrt{\rho}/\sqrt{t}$ when $\mu \equiv 0$.) Since there is clearly less mass between branches than at the tips, growth and side branching there gets stunted by increasing μ.

Realistic "classic" dendrites occur for a relatively narrow range of choices for μ, once the other parameters are held fixed. Typically, though, the other parameters need to be perturbed along with μ; increasing μ alone tends to erode all complex structure.

The markings seen on snow crystal plates are sometimes called *hieroglyphs*. These often have fairly regular geometric forms, such as ridges, flumes, ribs, and circular shapes, but can also exhibit more chaotic patterns. In photomicrograph collections [**BH**, **LR**, **Lib5**, **Lib6**] it is usually unclear whether the marks are on the outside of the crystal or within what we call sandwich plates. In our experiments, the inner structures are *much* more prevalent, so we are glad to observe that they are abundant in nature [**EMP**]. To obtain nice *outer* markings, the ratio β_{01}/β_{20} needs to be sufficiently large, but there is then a tendency for the crystal to become too three-dimensional. Again, the correct choice is often rather delicate. Inner markings occur generically for small values of this ratio.

Finally, different κ's may appear to be a more natural mechanism to enforce anisotropy than different β's, as they directly correspond to sticking, or *killing*, of particles at the crystal's boundary. However, for this effect to be significant, the killing at the boundary must be slow and thus the κ's need to be very close to 1; this causes the already slow growth to proceed at an even more sluggish pace. While less physically appealing, we view the β's as a reasonable compromise for the sake of computational efficiency.

6 Variants and extensions of the model

6.1 Uniform snowfakes

Since attachment thresholds β vary, the mass of the final crystal is not uniform. There is a variant of our algorithm that removes this defect with little change in observed morphology. Assume that there is no automatic filling of holes; instead, boundary mass exactly 1 is needed for attachment when $n_t^{\mathbb{T}}(x) \geq 4$ and $n_t^{\mathbb{Z}}(x) \geq 1$. Then a uniform crystal is obtained by performing the following additional step just after step *iii* in the simulator:

iii'. Post-attachment mass redistribution

To redistribute any excess mass from the attached site to its unattached neighbors, let

$$n_t^c(x) = \#\{y \in \mathcal{N}_x : a_t^\circ(y) = 0\}$$

be the number of non-attached neighbors. Then, for every x with $a_t^\circ(x) = 0$,

$$b_t'(x) = b_t^\circ(x) + \sum_{y : a_t^\circ(y) = 1} \frac{b_t^\circ(y) - 1}{n_t^c(y)}.$$

6.2 Simulation without symmetry

As explained in Section 3, at the cost of a 24-fold slowdown compared to our fully symmetric model, implementation of the algorithm without exploiting symmetry makes it possible to study the evolution from arbitrary initial seeds. Such an extension is necessary in order to produce snowfakes corresponding to exotic forms such as triangular crystals, split stars, and bullets. We have conducted a few experiments along these lines with our planar model [**GG3**], but in three dimensions a simulator dramatically faster than our current one is needed. We have future plans to develop a suitably high-performance parallel version.

6.3 Random dynamics

Our only three-dimensional snowfakes to date are deterministic, since randomness would also require the just discussed simulation without symmetry. We propose to include an additional parameter ϵ representing residual noise on the mesoscopic scale, as we did in the two-dimensional setting [**GG3**]. Again, ϵ would need to be quite small, say on the order 10^{-5}. The random perturbation of diffusive mass from [**GG3**] is not suitable in 3d since it is not physical to violate mass conservation. Instead, a small random slowdown in the diffusion rate is more appropriate. To this end, first denote the (linear) operation on the field d_t° in (1a–1c) by $\mathcal{D}$; thus step i can be written as $d_t''' = \mathcal{D}(d_t^\circ)$. Next, let $\xi_t(x)$, $t \geq 0$, $x \in \mathbb{T} \times \mathbb{Z}$, be independent random variables, equal to $\epsilon > 0$ or 0, each with probability 1/2. Here the field ξ represents the proportion of particles that refuse to diffuse at position x and time t.

The randomized step i now reads

$$d_t''' = \mathcal{D}((1-\xi_t)d_t^\circ) + \xi_t d_t^\circ = \mathcal{D}(d_t^\circ) + \xi_t d_t^\circ - \mathcal{D}(\xi_t d_t^\circ).$$

In a natural way, this represents small random temperature fluctuations in space and time.

Similarly, one could introduce a small proportion of particles that refuse to freeze in (2b), or melt in (4); e.g., (2b) would be replaced by

$$b_t'(x) = b_t^\circ(x) + (1-\kappa(n_t^{\mathbb{T}}(x), n_t^{\mathbb{Z}}(x)))d_t^\circ(x)(1-\xi_t(x)),$$
$$d_t'(x) = \kappa(n_t^{\mathbb{T}}(x), n_t^{\mathbb{Z}}(x))d_t^\circ(x)(1-\xi_t(x)) + d_t^\circ(x)\xi_t(x).$$

7 Case study i : ridges and plates

Our prototypical snowfake has $\rho = .1$ and the canonical initial state of radius 2 and thickness 1. Fig. 4 depicts the crystal after 70000 time steps, when its radius is about 350. Its parameters are $\beta_{01} = 2.5$, $\beta_{10} = \beta_{20} = \beta_{11} = 2$, $\beta_{30} = \beta_{21} = \beta_{31} = 1$, $\kappa \equiv .1$, $\mu \equiv .001$, and $\phi = 0$.

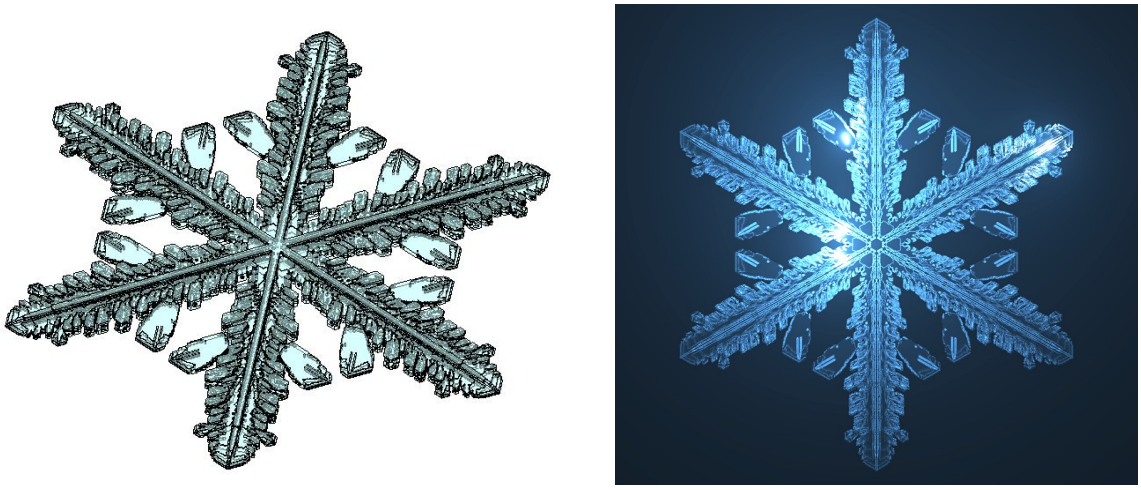

Fig. 4. The oblique (MATLAB-rendered) and top (ray-traced) views of the crystal.

We invite the reader to compare the simulated crystal with some of the photographs at [**Lib5**] and especially with Fig. 1(h) in [**TEWF**], a snowflake obtained at temperature about $-13°$C. We think of our length unit (the width of the fundamental prism) as about 1μm, so even the sizes of the two objects roughly match.

Perhaps the most striking features shared by the snowfake in Fig. 4 and physical ones are the *ridges*, elevations in the middle of each main branch, with less pronounced counterparts on the side branches. We begin by illustrating how these ridges are formed and maintained. In the process we also encounter the *branching instability*, when the initial growth of a thin hexagonal plate is no longer viable and it gives birth to the six main branches.

As shown in Fig. 5, ridges are formed quite early in the evolution, by mesoscopic bumps known as *macrosteps* that are near the center of the plate. This is how the ridges grow (*very* slowly) in the vertical direction — compare with times 4044 and 7099, which also feature such bumps. The ridges spread to a characteristic width, but sharpen to a point near the branch tip. One can also observe the commonly observed *flumes* (called *grooves* in [**Lib6**]) that form on both sides of a ridge.

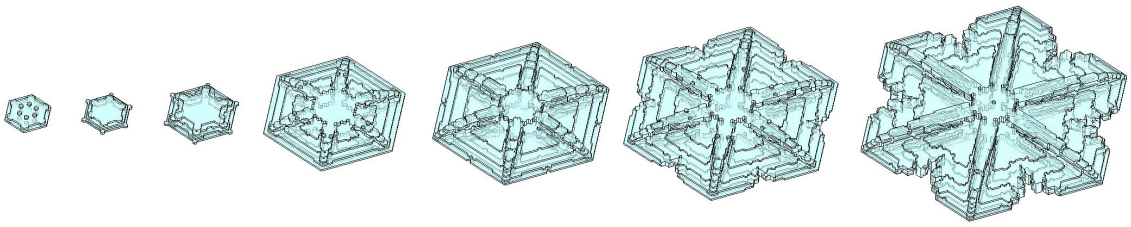

Fig. 5. The crystal at times 820, 863, 1600, 4044, 5500, 7099, and 9500.

The small indentation that emerges, due to lower vapor density, in the middle of each prism facet at time 5500, has appeared several times before. However, this is the first instance when the growth is unable to repair it. Instead, the growth there virtually stops, while the six main arms continue to grow and eventually produce two types of side branches: common, relatively thick double-plated branches that we call *sandwich plates*, and more unusual thin plates with their own ridges. The tip of each arm assumes its characteristic shape by the final frame of Fig. 5.

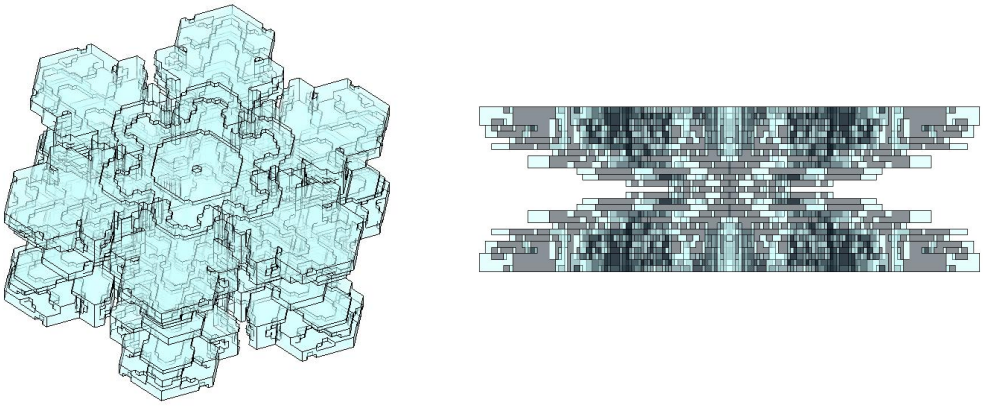

Fig. 6. Oblique and side views of the crystal from a different initial state.

It is perhaps surprising how dramatically this scenario depends on the initial (micron scale) state. Keeping everything else the same, we change the initial prism to one with radius 2 and thickness 3. The previous rather complex and aesthetically pleasing evolution is replaced by a growing double plate (Fig. 6). (Remarkably, even adding a small drift does not help matters much.) This dichotomy arises frequently in our model — within a neighborhood of the parameter space that produces planar crystals there are two stable attractors: one with outside ridges and the other a split plate with ridges on the inside. As much of the literature points out, split plates are extremely common in physical crystals (cf. [**Iwa**]).

Finally, let us experiment with changing the density ρ. We exhibit five crystals, each with the canonical initial condition and all other parameters of the prototype unchanged, but at different densities and different final times. Dramatically lower density does promote faceting ([**Lib6**, **LR**]), but a moderate perturbation seems to mainly promote slower growth, without a change in morphology.

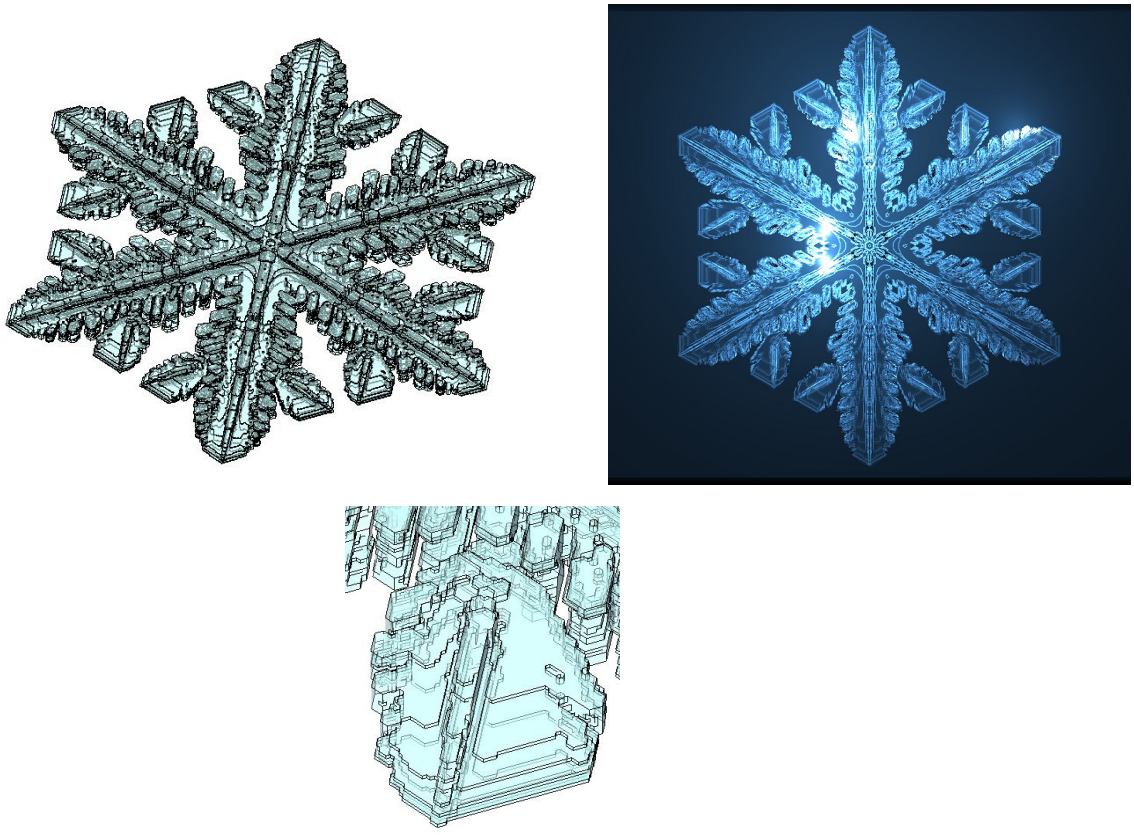

Fig. 7. At density $\rho = .15$, the side branches have particularly well-defined ridges.

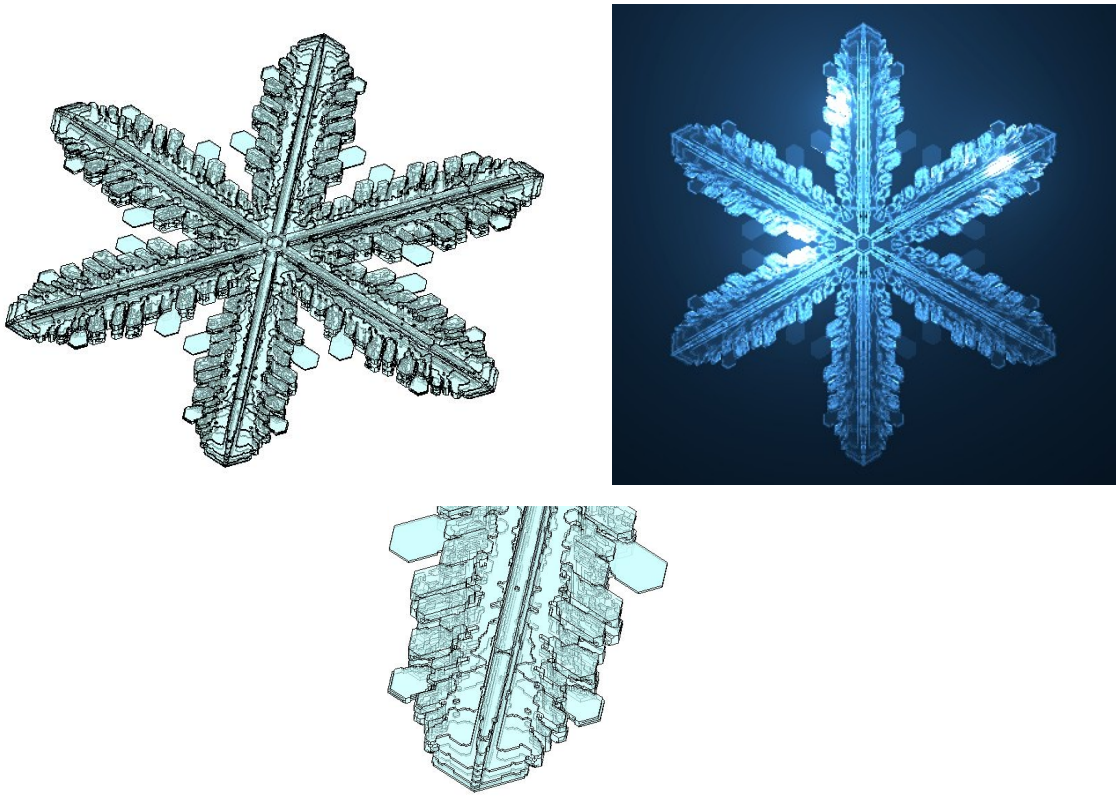

Fig. 8. At density $\rho = .09$, the flumes are well-delineated.

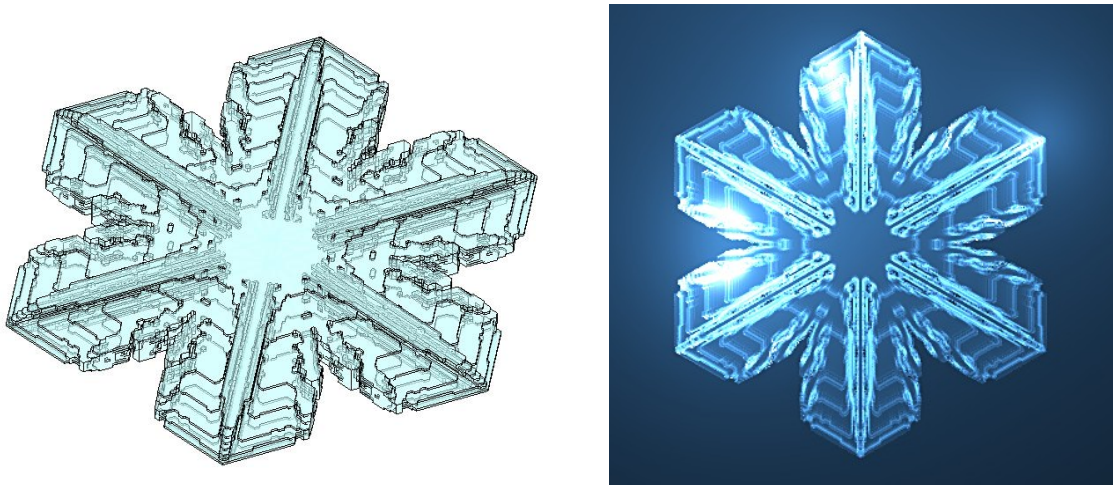

Fig. 9. Density $\rho = .05$ results in sectored plates.

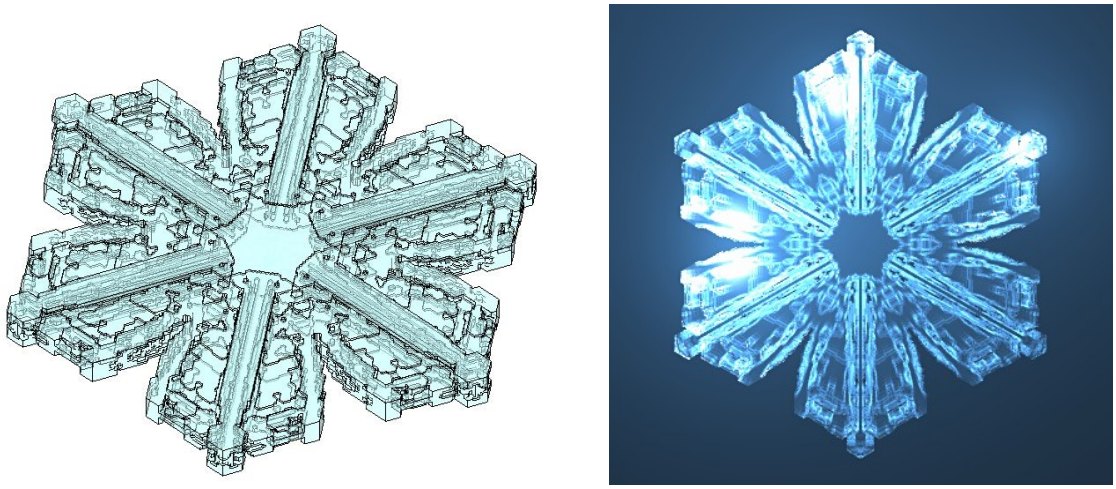

Fig. 10. Density $\rho = .045$ results in sectored branches.

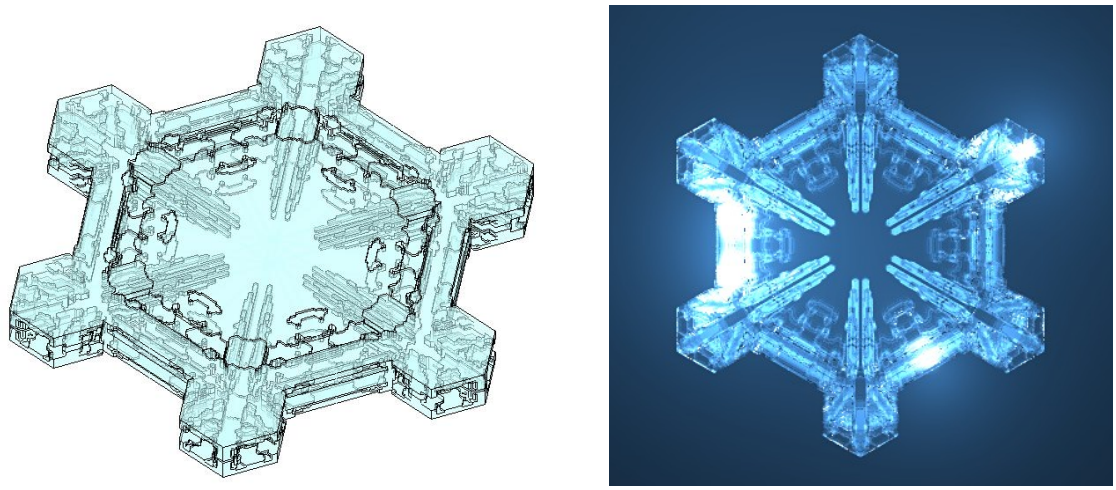

Fig. 11. Density $\rho = .4$ results in sandwich plates with inner ridges.

The example in Fig. 11 (pictured at time 120000) never undergoes the branching instability illustrated in Fig. 5, although it does develop fairly standard ridges that persist until about time 40000. This is the time shown in the first frame of Fig. 12; subsequent frames show the evolution in time increments of 10000. We observe that a completely different *sandwich instability* takes place: first the tips and then the sides of the snowfake thicken and develop sandwich plates. It is also clear from the time sequence that this morphological change is accompanied by a significant slowdown in growth. We should emphasize that this slowdown is *not* due to the depletion of mass

on a finite system: much larger systems give rise to the same sandwich instability well before the edge density diminishes significantly. Neither is this slowdown accompanied by a significant growth in the $\mathbb{Z}$-direction — in the period depicted, the radius in the $\mathbb{Z}$-direction increases from 6 to 7, whereas the radius in the $\mathbb{T}$-direction increases from 67 to 87. Instead, much of the growth fills space between the ridges, the remnants of which end up almost completely below the surface.

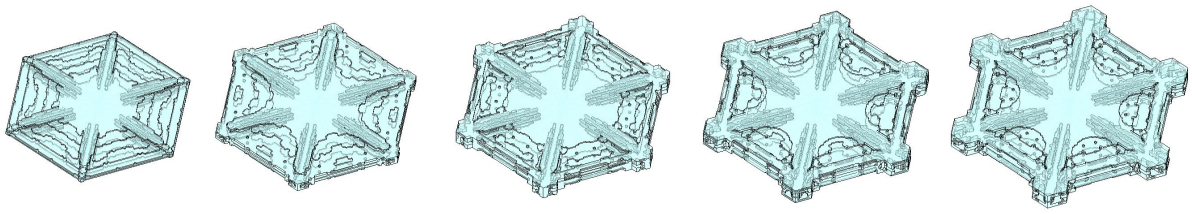

Fig. 12. The crystal of Fig. 11 at earlier times.

Note that the snowfake of Fig. 10 is also experiencing the sandwich instability at about the capture time. The difference in that case is that the growing crystal also experienced the branching instability earlier in its development.

8 Case study *ii* : classic dendrites

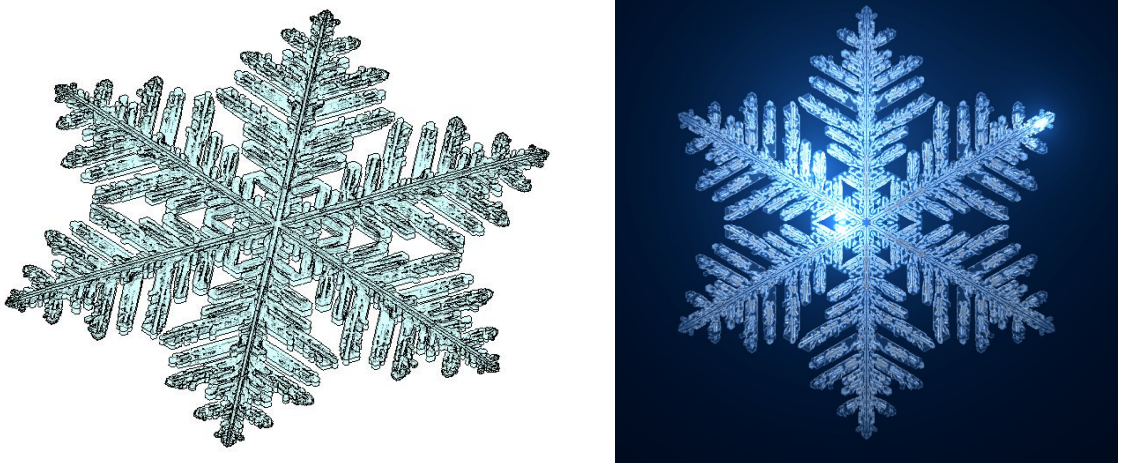

Fig. 13. $\rho = .105$: a fern dendrite.

For this series of snowfakes, $\beta_{01} = 1.6$, $\beta_{10} = \beta_{20} = 1.5$, $\beta_{11} = 1.4$, $\beta_{30} = \beta_{21} = \beta_{31} = 1$, $\kappa \equiv .1$, all $\mu \equiv .008$, $\phi = 0$, and growth starts from the canonical initial state. We will again look at how morphology is affected by different vapor densities ρ. The simulations argue persuasively that the frequency of side branches decreases with decreasing ρ. When $\rho = .105$, the branches are so dense that the crystal is rightly called a fern, while the examples with $\rho = .1$

and $\rho = .095$ have the classic look of winter iconography. These are our largest crystals, with radii around 400. A more substantial decrease in ρ eliminates any significant side branching on this scale, resulting in a simple star for $\rho = .09$. As should be expected from Section 7, further decrease finally produces a sandwich instability at the tips, resulting in thick double plates. In this instance, slow growth at the branch tips is accompanied by significant fattening in the $\mathbb{Z}$-direction.

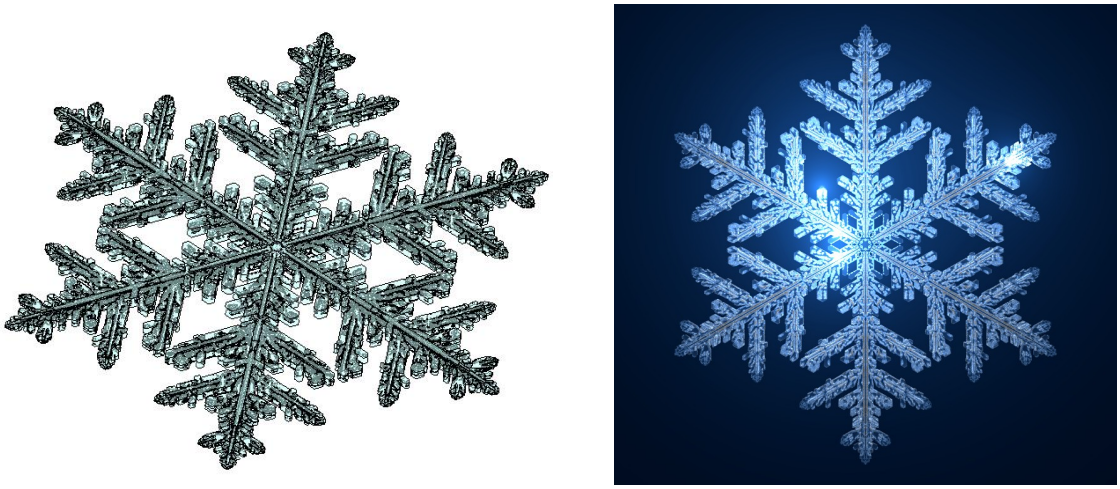

Fig. 14. $\rho = .1$: a classic dendrite.

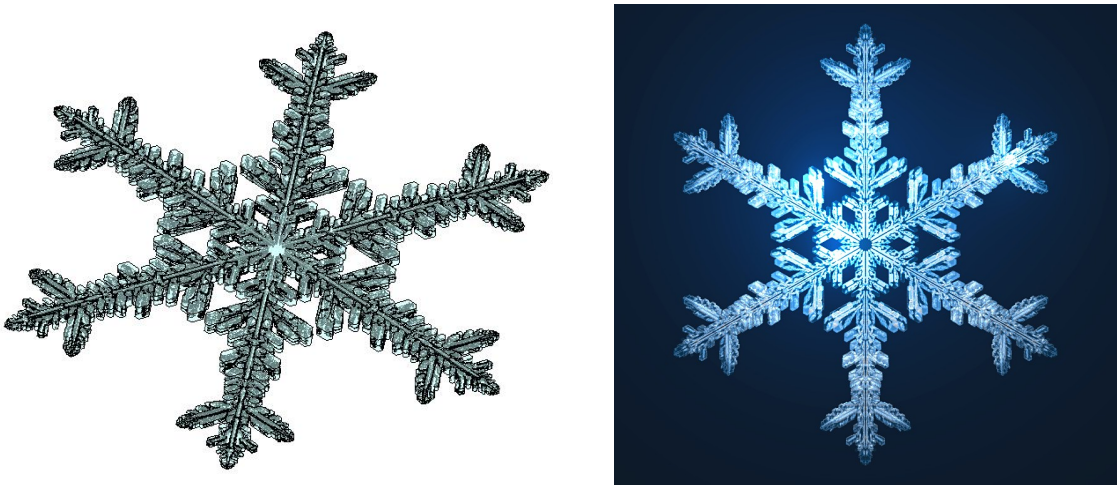

Fig. 15. $\rho = .095$: fewer side branches.

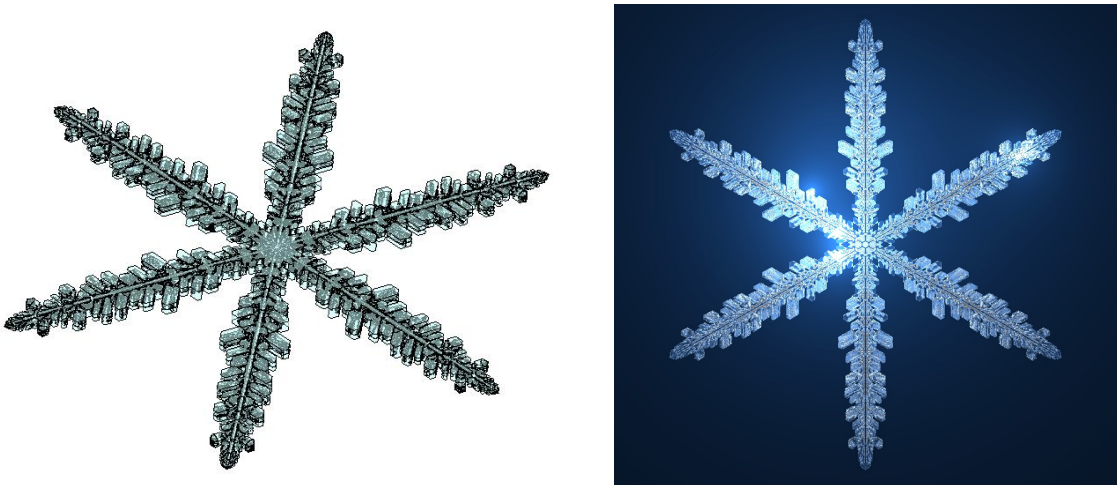

Fig. 16. $\rho = .09$: no significant side branches on this scale.

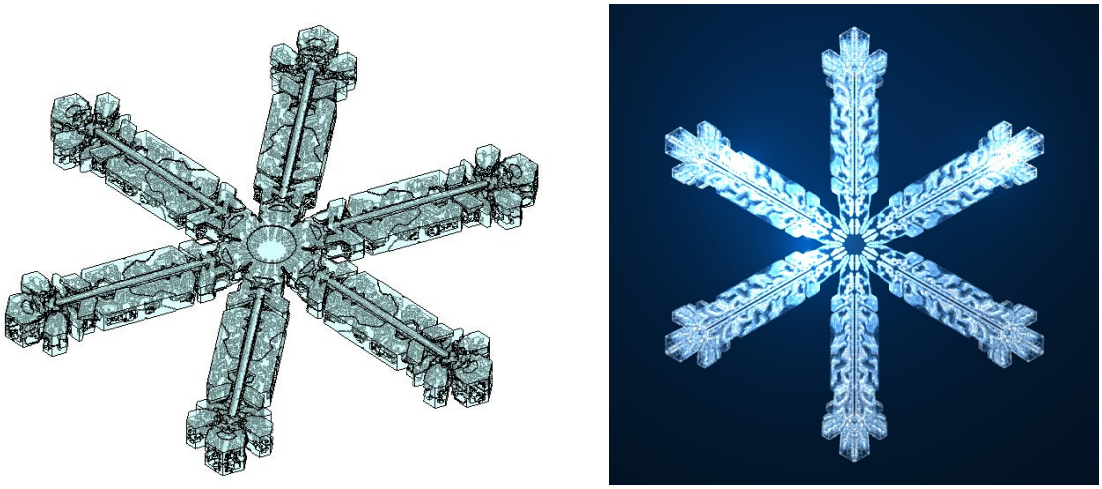

Fig. 17. $\rho = .082$: the tip undergoes a sandwich instability.

The crystal in Fig. 17 is captured at about time 60000. The series of close-ups in Fig. 18 provides another illustration of the sandwich instability — snapshots of the same snowfake are shown at time intervals of 1000, starting from time 37000.

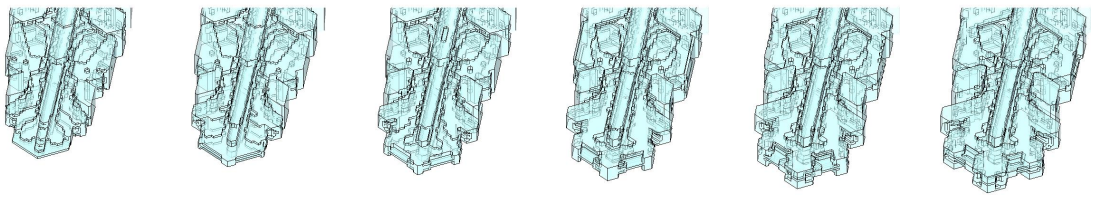

Fig. 18. Close-up of the sandwich instability at $\rho = .082$.

Our final example, with $\rho = .081$, demonstrates that a further decrease in density makes the crystal increasingly three-dimensional.

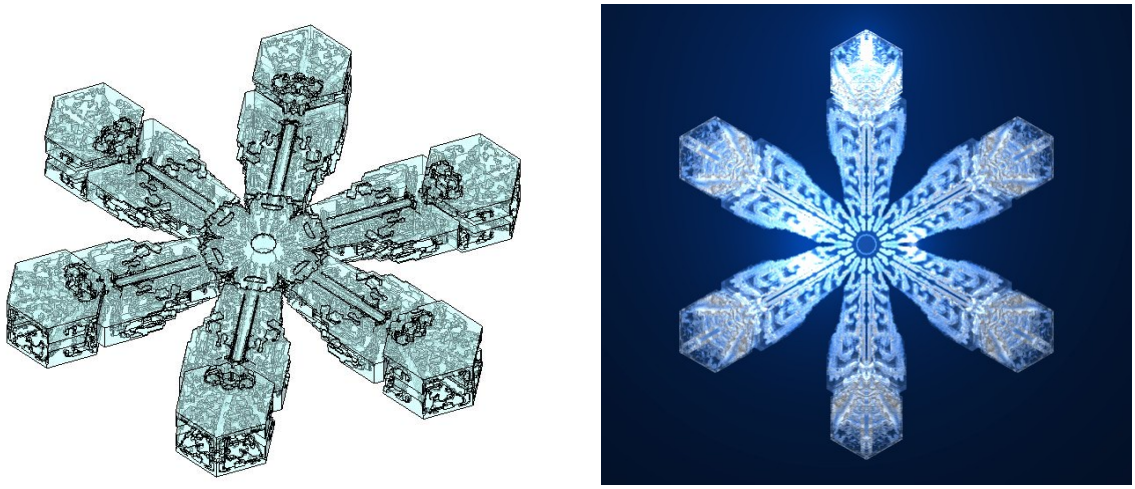

Fig. 19. Fattening from the tip inward at $\rho = .081$.

9 Case study *iii* : sandwich plates

When growth in the $\mathbb{Z}$-direction is much slower than in the xy-plane, outer ridges never develop. Instead, the dynamics grows a featureless prism, which, when sufficiently thick, undergoes a sandwich instability producing inner ridges. Much later the crystal experiences the branching instability, with plate-like branches that bear a superficial resemblance to Packard snowflakes [**Pac**, **GG2**] during early stages.

Throughout the evolution the external surface of the crystal has few markings, whereas inside features include ridges and *ribs*, which signify gradual thinning of the plates from the center outward before the branching instability.

The sole surface designs are *reverse shapes*, which occur when the crystal grows in the $\mathbb{Z}$-direction from buds that arise close to the tips. These macrostep nuclei result in rapid growth of a single layer in the $\mathbb{T}$-direction until this layer outlines a nearly circular hole near the crystal's center; the hole then proceeds to shrink much more slowly.

We note that this observation provides a convincing explanation for the circular markings seen on many snow crystal photographs [**Lib6**, **LR**]. It also suggests that ribs are predominantly inner structures. While outer ribs could occur due to instabilities or changing conditions (cf. Fig. 11), there is scant evidence of them in electron microscope photographs [**EMP**], which completely obscure inner structure. On the other hand, those photos reveal an abundance of sandwich plates, which appear as the crystal centers, at the tips of the six main arms, and as side branches.

We now present two examples. Both start from the canonical seed. In the first, depicted in Fig. 20, $\beta_{01} = 6$, $\beta_{10} = \beta_{20} = 2.5$, $\beta_{11} = 2$, and the remaining β's are 1. All κ's are .1, except

that $\kappa_{01} = .5$, $\mu \equiv .0001$, and $\rho = .08$. The final radius of the crystal at the capture time 100000 is about 150. Note that the main ridge is interrupted: while initially it connects the two plates (and it has darker color in the ray-traced image as the background can be seen through it), it later splits and each plate has its own ridge. There is a suggestion of this phenomenon in real crystals (e.g., on p. 26 of [**Lib6**]).

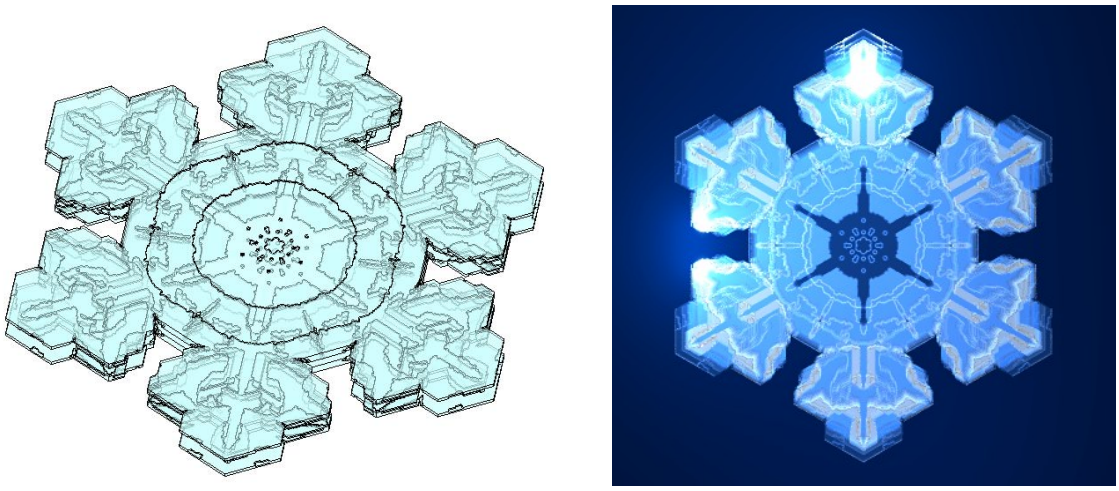

Fig. 20. A sandwich plate.

Our second example (Figs. 21 and 22) has interrupted main ridges and a few ribs. The parameter set now has $\beta_{01} = 6.5$, $\beta_{10} = \beta_{20} = 2.7$, and $\rho = .15$. The remaining values are as before, and the final sizes (this one at $t = 36100$) are comparable. We provide a few intermediate stages and a detail of the inner structure. Observe the buds at times 25883 and 31671; also note that the outermost rib at time 19000 later disappears.

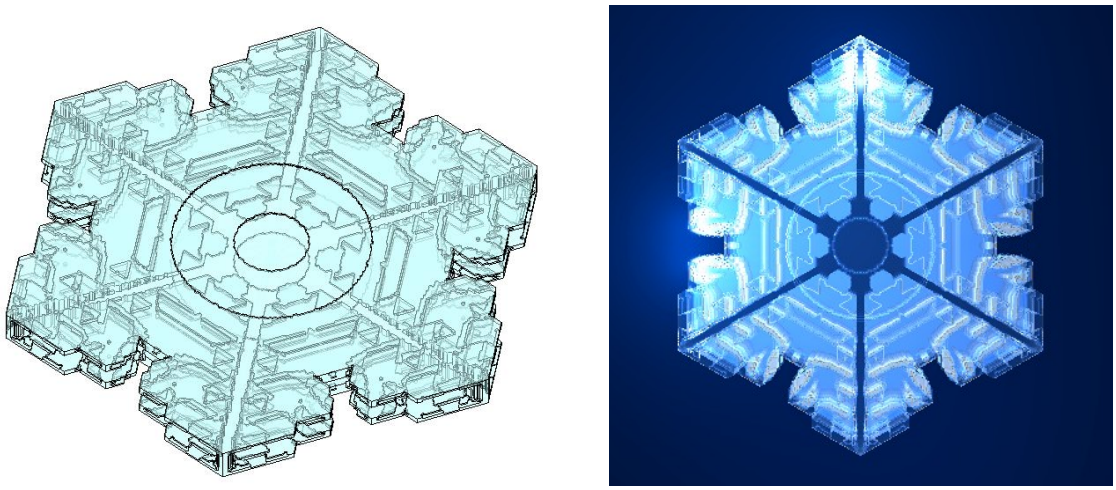

Fig. 21. Another sandwich plate.

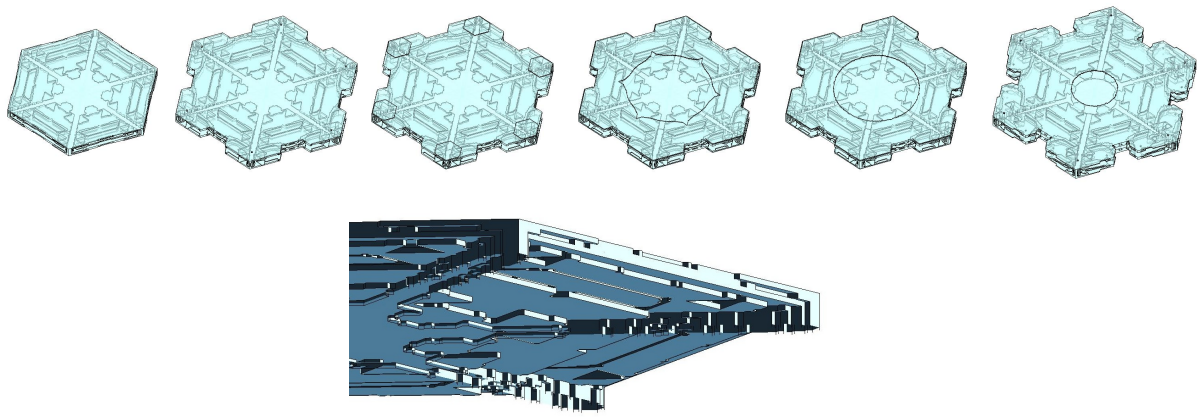

Fig. 22. The plate of Fig. 21 at $t = 19000, 25883, 25900, 25950, 26000, 31671$. The detail is from the first time, obtained by cutting the crystal along the plane $z = 0$ and zooming in on the bottom half of the upper portion.

10 Case study *iv*: the roles of drift and melting

From some of the electron micrographs at [**EMP**], it appears possible that the basal facets may have ridges and other markings on one side only, while the other side is nearly featureless. As far as we are aware, no attempt has been made to "turn over" these specimens and confirm the asymmetry, but [**NK**, **Nel**] offer a theoretical explanation. They suggest that the one-sided structure is a consequence of early growth and that ridges are actually vestiges of the skeleton of hollow prisms such as Fig. 31 in Section 11 (see Fig. 3 of [**Nel**]). In fact, it is widely held that the micron-scale prism from which a prototypical snowflake evolves develops slight asymmetries in the radii of its two basal facets, and that the larger facet acquires an increasing advantage from the feedback effect of diffusion-limited growth. As a result many crystals have a stunted hexagonal plate at their center. In [**Nak**] this effect is described on p. 206 and in sketch 15 of Fig. 369.

Another potential source of asymmetry in the $\mathbb{Z}$-direction is identified in Section 3.5 of [**Iwa**] and on p. 18 of [**TEWF**], based on cloud tunnel experiments in the laboratory. Planar snowflakes evidently assume a preferred orientation parallel to the ground as they slowly fall, resulting in a small upward drift of the diffusion field relative to the crystal.

We emulate these aspects of asymmetric growth by means of the drift ϕ in step (1c) of our algorithm and asymmetry of the initial seed as mentioned in Section 3. Consider first the snowfake of Fig. 1 and the closely related sectored plate in Fig. 23. The former starts from our fundamental prism and never undergoes the sandwich instability, but develops ridges on the bottom side and an almost featureless top due to the presence of $\phi = .01$. The dynamic parameters of the sectored plate below are identical, but growth starts from a mesoscopic prism that is 5 cells high, with radius 7 at the top and 3 at the bottom. The idea here is to mimic the situation where the upper basal plate has established an advantage over the lower basal plate early in the evolution. As is clear from the side view, in contrast to Fig. 6, growth of the lower facet stops completely due to diffusion limitation even though the small drift offers

a slight advantage in the early stages. (According to [**Iwa**], falling snowflakes prefer the more aerodynamically stable orientation of Fig. 23.) Very many photos of physical snow crystals show evidence of such a stunted simple plate at the center; see [**Lib6**], pp. 75–76, for further discussion.

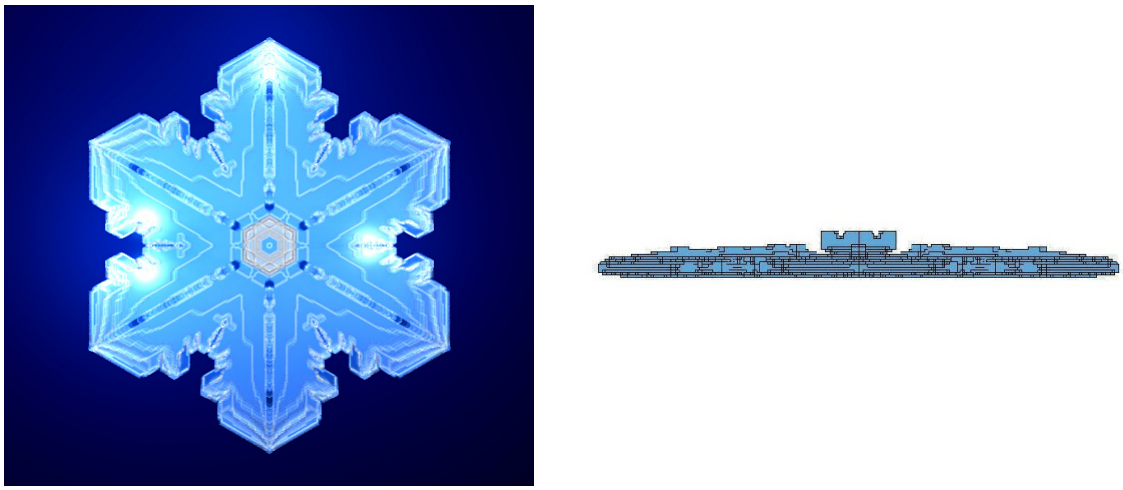

Fig. 23. A sectored plate with a stunted double, from the top (*left*) and side (*right*).

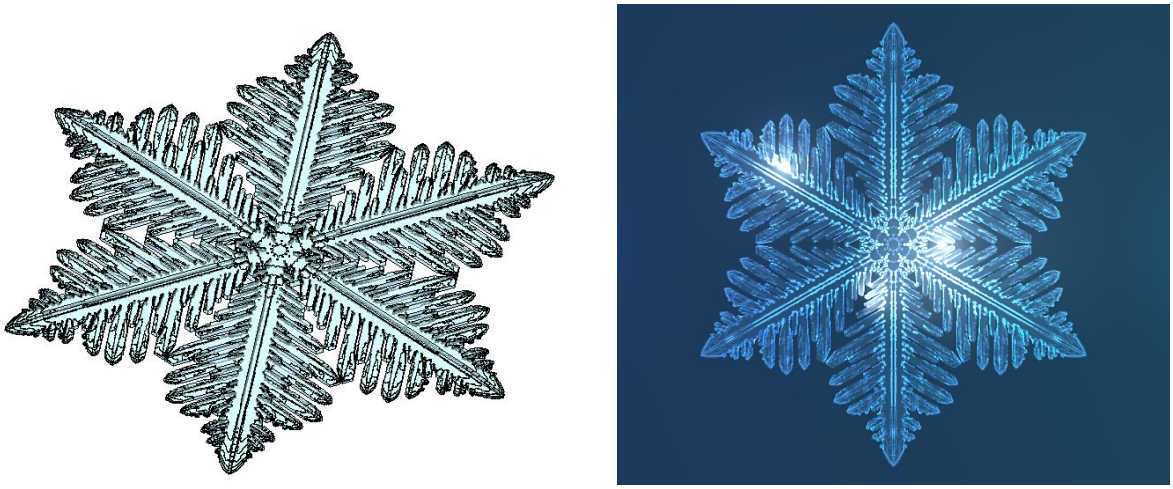

Fig. 24. A fern dendrite for $\mu_{10} = \mu_{20} = .005$.

The remaining examples of this section also start from slightly asymmetric seeds, experience a small drift, and have almost all their external markings on one side. Our goal is to explore the role of the melting rate, in much the same way we studied density dependence in Section 7, by varying μ in a series of snowfakes with all other parameters held fixed. In each instance, the seed has height 3, lower radius 2, and upper radius 1. For the next four crystals, $\beta_{01} = 3$, $\beta_{10} = \beta_{20} = \beta_{11} = 1.4$, $\beta_{30} = \beta_{21} = \beta_{31} = 1$, $\kappa \equiv .1$, $\phi = .01$, and $\rho = .14$. Moreover $\mu_{01} = .002$, $\mu_{30} = \mu_{11} = \mu_{21} = \mu_{31} = .001$ and we vary only the common value of $\mu_{10} = \mu_{20}$. This value

governs the speed of tips and — as explained in Section 5 — has more effect in regions of low density, so an increase inhibits side branching.

Like the sectored plates just discussed, these are relatively rare snowfakes with outside ridges on the main arms and most side branches. All our modeling experience suggests that crystal tips tend to symmetrize with respect to the $\mathbb{T}$-direction, managing to avoid the sandwich instability only under quite special environmental conditions. We have seen little evidence in our simulations for the mechanism of ridge formation proposed in [**NK**, **Nel**], so we feel that drift is a more likely explanation of one-sided structures in snowflakes.

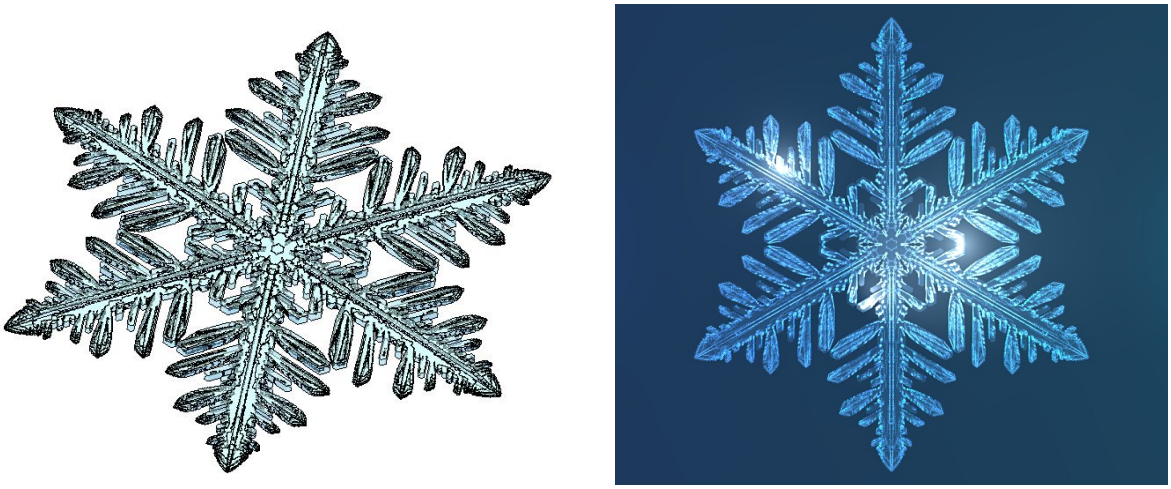

Fig. 25. Reduced side branching for $\mu_{10} = \mu_{20} = .008$.

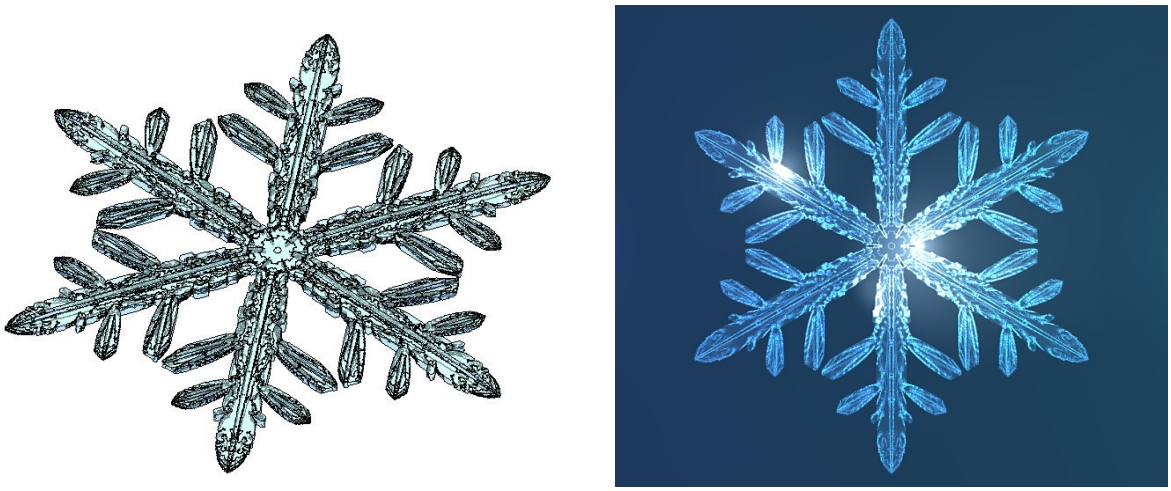

Fig. 26. Further reduction in the number of side branches for $\mu_{10} = \mu_{20} = .009$.

Starting with the classic fern of Fig. 24, the common prism facet melting threshold $\mu_{10} = \mu_{20}$ is gradually increased to twice the original value in Figs. 25–7. Stellar dendrites with fewer and fewer side branches result, until the final snowfake has only a few short sandwich plates on the sides of each arm.

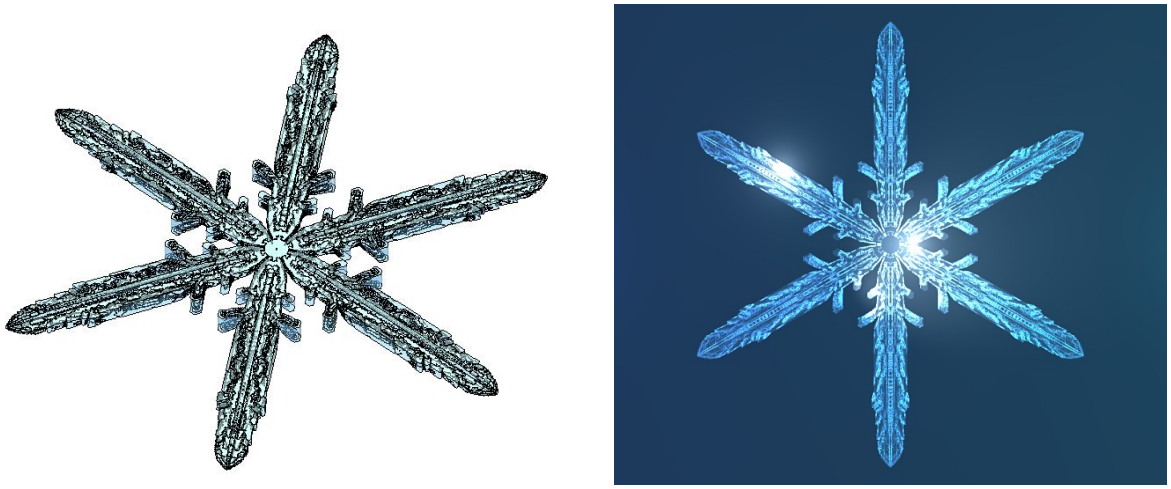

Fig. 27. When $\mu_{10} = \mu_{20} = .01$, very few side branches remain.

The final example of this section is a classic simple star, a crystal with no side branches at all and a characteristic parabolic shape to its tips (cf. [**Lib6**], p. 57 bottom). This elegant snowfake required considerable tweaking of parameters; they are: $\beta_{01} = 3.1$, $\beta_{10} = 1.05$, $\beta_{20} = 1.03$, $\beta_{11} = 1.04$, $\beta_{30} = 1.02$, $\beta_{21} = 1.01$, $\beta_{31} = 1$, $\kappa \equiv .01$, $\mu_{01} = \mu_{30} = \mu_{11} = \mu_{21} = \mu_{31} = .01$, $\mu_{10} = \mu_{20} = .03$, $\phi = .005$, and $\rho = .16$.

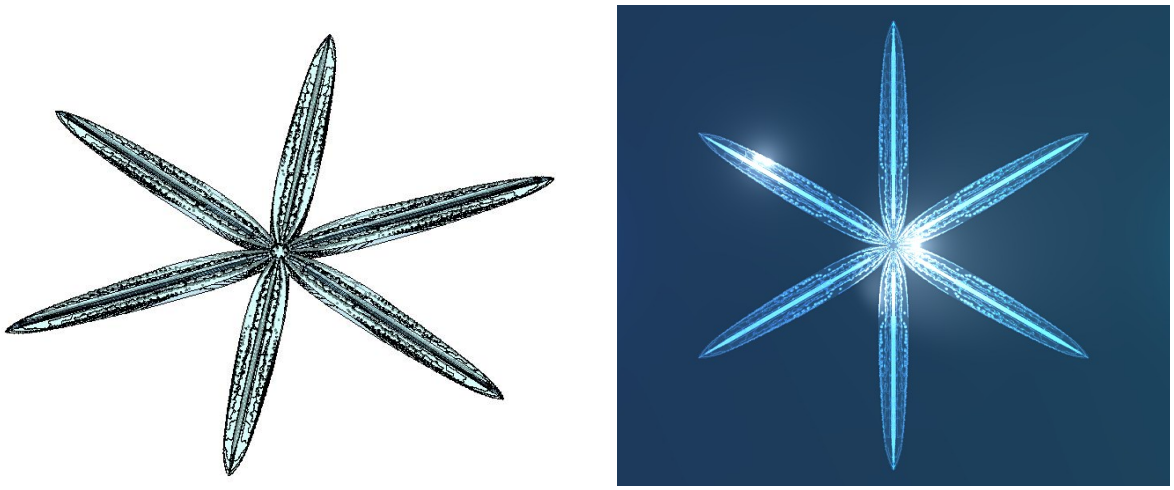

Fig. 28. A simple star.

11 Case study v : needles and columns

Let us now turn to the common but less familiar snow crystals that expand primarily in the $\mathbb{Z}$-direction. As one would expect, these have β_{01} small compared to β_{10} and β_{20}, but surprisingly small advantage often suffices. We offer three snowfakes that emulate their physical counterparts quite well. All start from the canonical seed. Our first example, with a substantial bias toward attachment on the basal facets, is a (simple) *needle*. In Fig. 29, $\beta_{01} = 2$, $\beta_{10} = \beta_{20} = \beta_{11} = 4$, $\beta_{30} = \beta_{21} = \beta_{31} = 1$, $\kappa \equiv .1$, $\mu \equiv .001$, $\phi = 0$, and $\rho = .1$. This snowfake reproduces structure observed in nature and the laboratory: slender hollow tubes, often with cable-like protuberances at the ends (cf. Fig. 135 of [**Nak**], pp. 67–68 of [**Lib6**]).

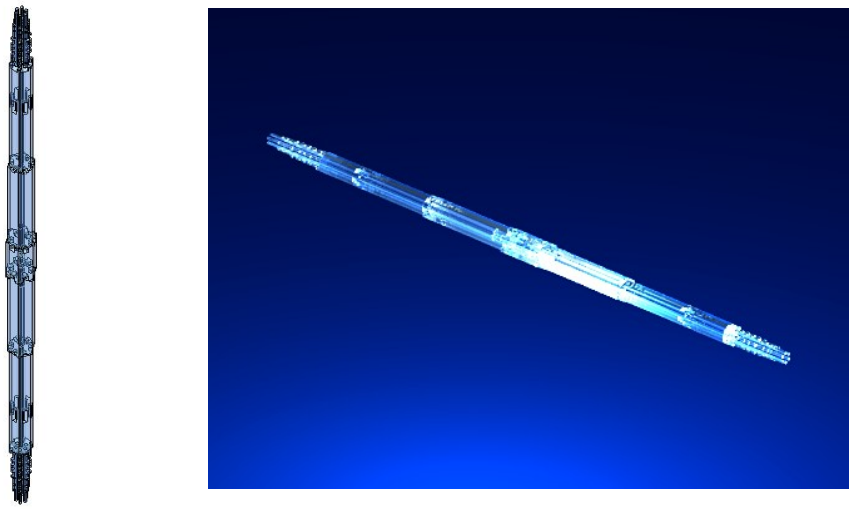

Fig. 29. A needle.

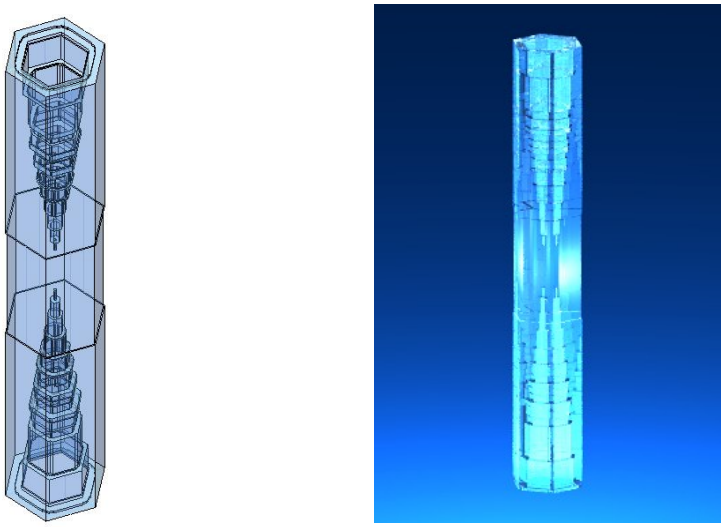

Fig. 30. A hollow column.

Next, Fig. 30 simulates the common type of snow crystal known as a *hollow column*. Here the bias toward attachment on the basal facets is not as pronounced. The parameter set is: $\beta_{01} = 1$, $\beta_{10} = \beta_{20} = 2$ $\beta_{30} = \beta_{11} = \beta_{21} = .5$ $\beta_{31} = 1$, $\kappa \equiv .1$, $\mu \equiv .01$, $\phi = 0$, and $\rho = .1$. Evidently, the hole starts developing early on. See pp. 64–66 of [**Lib6**]) for photos of actual hollow columns and a qualitative description of their growth.

The final example of this section is a column whose facets are hollow as well. The morphology of Fig. 31 occurs when the rates of expansion in the two directions are not very different. Photos and a description of this sort of snowflake appear on pp. 35–37 of [**Lib6**]. Here $\beta_{01} = 1.5$, $\beta_{10} = \beta_{20} = 1.6$ $\beta_{11} = \beta_{30} = \beta_{21} = \beta_{31} = 1$, $\kappa \equiv .1$, $\mu \equiv .015$, $\phi = 0$, and $\rho = .1$.

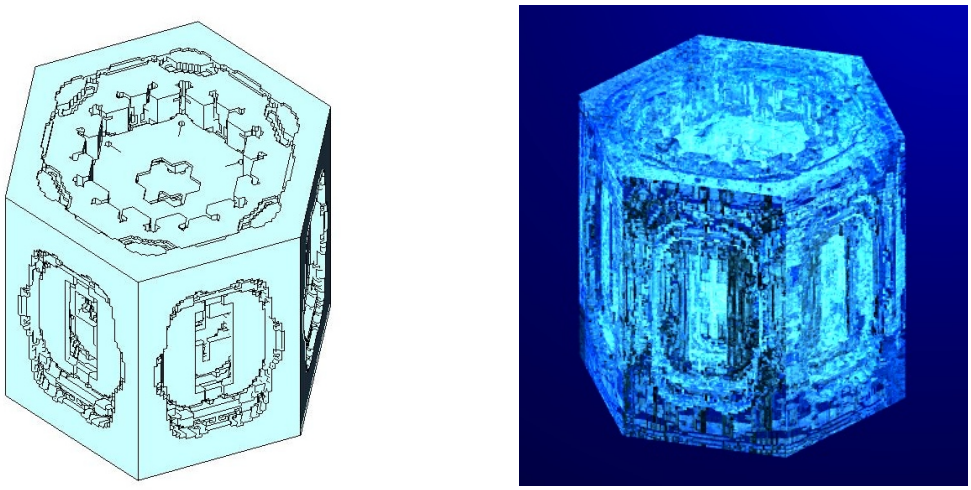

Fig. 31. A column with hollow prism facets.

12 Case study *vi* : change of environment

In his pioneering research, Nakaya [**Nak**] reproduced several of the most striking types found in nature by subjecting the cold chamber in his lab to a precisely controlled schedule of temperature and humidity changes, either sudden or gradual. Based on such experiments, he argued that *plates with dendritic extensions*, for example, are formed when a snowflake's early growth occurs in the upper atmosphere and then it drops to another layer more conducive to branching ([**Nak**], p. 16).

In this section we mimic such varying environments by consider the effect of an abrupt change of parameters on some of our previous snowfakes. Let us begin with two examples of the type cited in the last paragraph: plates with dendritic extensions. Both start from a prism that is 3 cells high with radius 2 at the top and 1 at the bottom. The first stage for both is a simple plate similar to the snowfake of Fig. 1, but with a delayed branching instability. The initial parameters are: $\beta_{01} = 3.5$, $\beta_{10} = \beta_{20} = \beta_{11} = 2.25$, $\beta_{30} = \beta_{21} = \beta_{31} = 1$, $\kappa \equiv .005$, $\mu \equiv .001$, $\phi = .01$, and $\rho = .12$. The first stage runs until time 8000 in the first example, and until time 12500 in the second. At that time most parameters remain the same, but in order to promote

branching we change $\beta_{10} = \beta_{20} = \beta_{11}$ to 1.15 (resp. 1.4) and $\mu_{10} = \mu_{20}$ to .006 (resp. 004). The results, once the two snowfakes have reached a radius of 200 cells, are shown in Figs. 32–3. Predictably, the first example has more branching in its dendritic phase since the prism facet attachment threshold is lower. The large image on the cover of [**Lib6**] shows a beautiful natural example of this type.

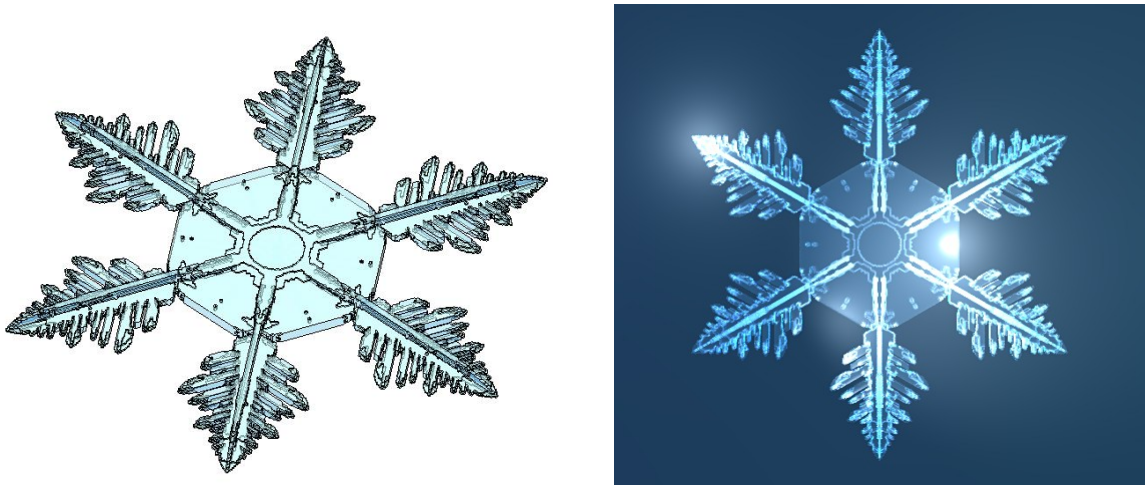

Fig. 32. A plate with fern extensions.

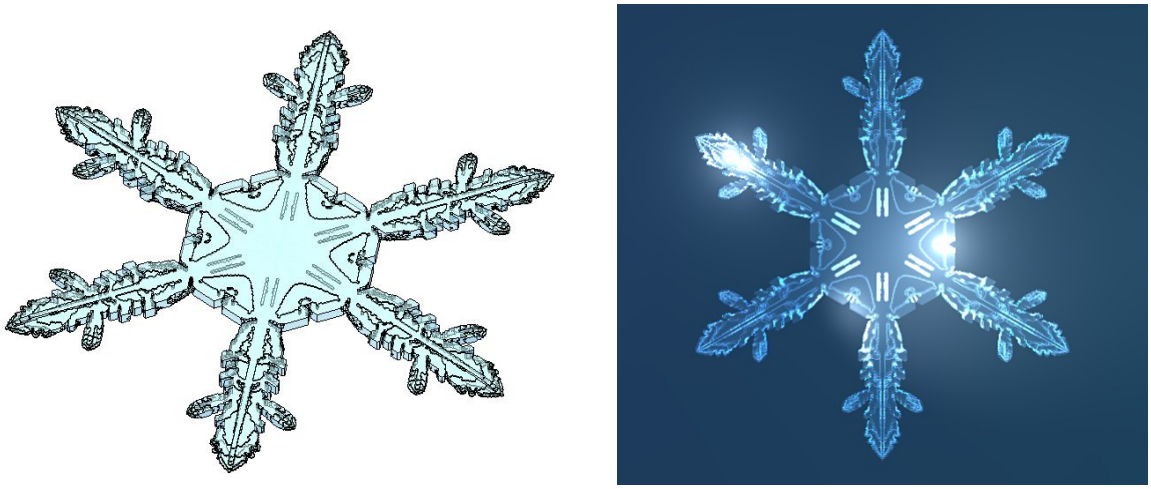

Fig. 33. A plate with dendrite extensions.

A hybrid evolution at the opposite end of the spectrum is described in [**Lib6**], pp. 51–53, and many of the most striking snowflakes in [**LR**] are of this type. As presumably in

nature, conditions need to be just right for the corresponding snowfake to evolve. In this vein, we present three snowfakes that begin as stellar dendrites with minimal branching and later encounter an environment promoting plates. All start from a prism of height 5 with top radius 6 and bottom radius 2. The first stage runs the simple star dynamics of Fig. 28 until time 4000, 3000, or 2000, respectively. Then new parameters for the three experiments with higher attachment thresholds are run until time, respectively, 24000, 20000, and close to 20000. Common parameters are: $\beta_{30} = \beta_{31} = 1$, $\kappa \equiv .1$, $\rho = .16$. In Fig. 34, the remaining parameters are $\beta_{01} = 3.0$, $\beta_{10} = \beta_{20} = 2.2$, $\beta_{11} = 2.0$, $\beta_{21} = 1.1$, $\mu \equiv .01$, $\phi = .005$. Note that in this instance the branches of the star broaden considerably after the change of environment, and the tips form sandwich plates.

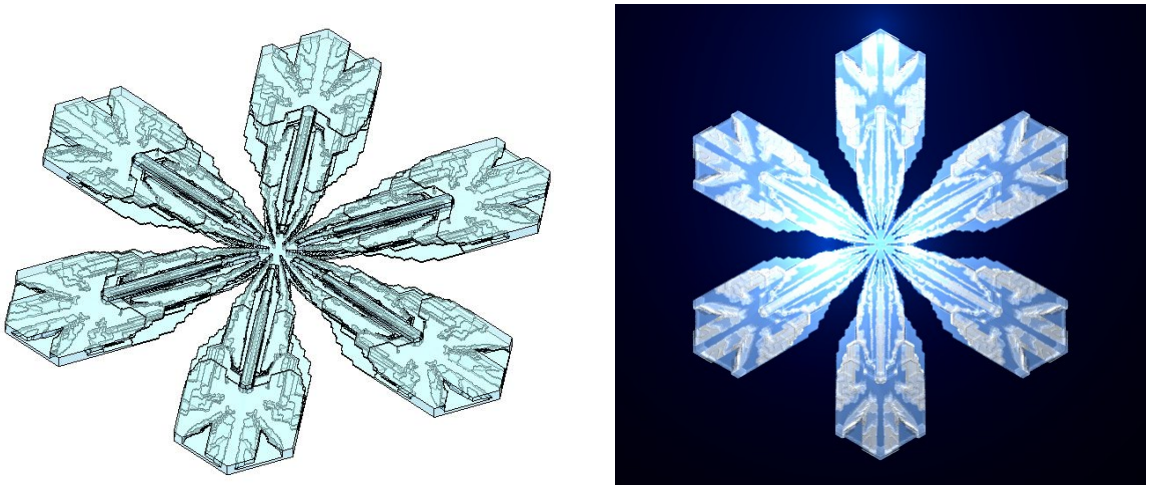

Fig. 34. A broad-branched stellar crystal with sandwich-plate extensions.

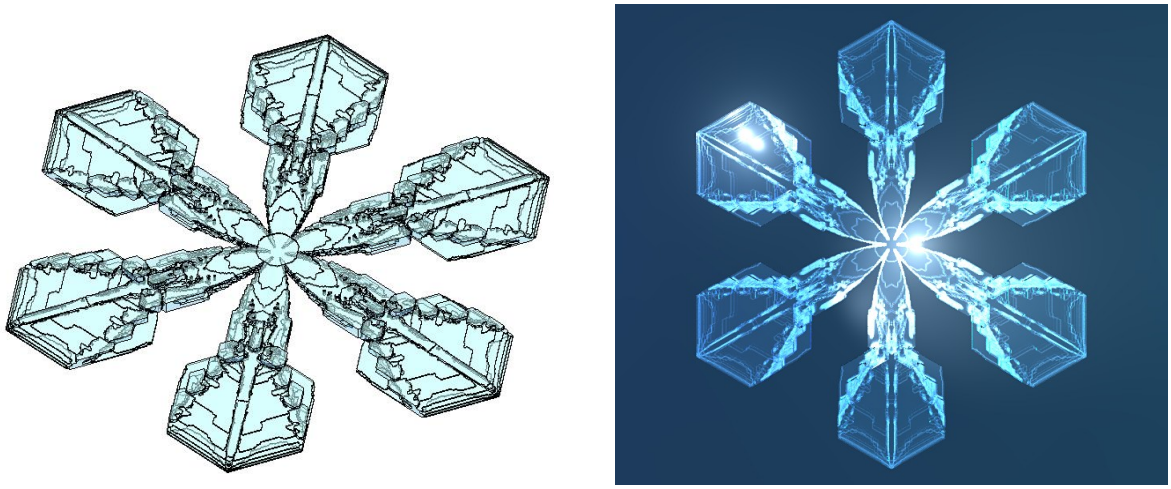

Fig. 35. A broad-branched stellar crystal with sectored-plate extensions.

By raising the attachment thresholds somewhat we avoid the sandwich instability and obtain instead the sectored-plate extensions with outside ridges seen in Fig. 35. Here $\beta_{01} = 3.5$, $\beta_{10} = \beta_{20} = 2.45$, $\beta_{11} = 2.25$, $\beta_{21} = 1.1$, $\mu_{10} = \mu_{20} = .002$, $\mu = .001$ otherwise, $\phi = .015$.

Our final broad-branched example interpolates between the previous two. The values of β are large enough to avoid the sandwich instability, but small enough that side branching leads to sectored plate structure of the extensions. Here $\beta_{01} = 3.0$, $\beta_{10} = \beta_{20} = 2.25$, $\beta_{11} = 2.05$, $\beta_{21} = 1.05$, $\mu \equiv .001$, $\phi = .015$.

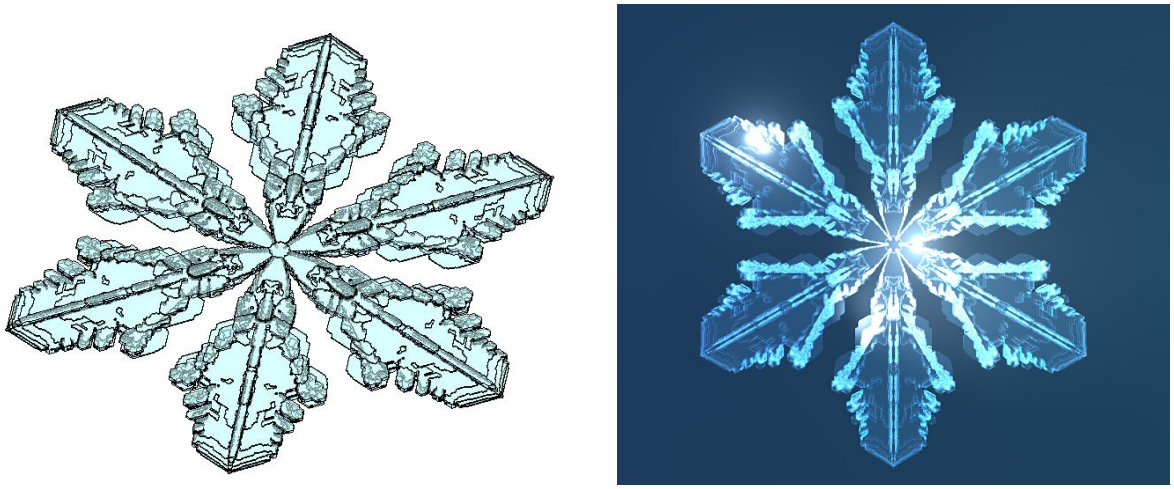

Fig. 36. Another broad-branched stellar crystal.

We conclude this case study with two crystals that combine a three-dimensional column and two-dimensional plates. These are the *tsuzumi*, or *capped columns*, described on pp. 69–74 of [**Lib6**]. They are thought to arise when crystals are transported to higher and colder regions of the atmosphere by a passing storm. Without a preferred orientation, it is most reasonable to model these as driftless. Both our snowfakes use the canonical seed and evolve with the parameters for the hollow column of Fig. 30 until time 20000. Then they run with new parameters that promote planar growth, until time 80000 for the first example, 60000 for the second. Common values for the two examples are: $\beta_{01} = 5$, $\beta_{30} = \beta_{21} = \beta_{31} = 1$, $\kappa \equiv .1$, $\mu \equiv .001$, $\phi = 0$, and $\rho = .1$. The difference is the common value $\beta_{10} = \beta_{20} = \beta_{11}$, which is 2.4 in Fig. 37, and 2.1 in Fig. 38. Higher attachment thresholds delay the branching instability in the first capped column so the caps are simple plates, as opposed to sectored plates in the second.

The transition period from column to cap in lab tsuzumi is described in some detail by Nakaya ([**Nak**], p. 221; see also the sketch on p. 222). We remark that our snowfake versions evolve in the same way. Namely, for a considerable time after the change of environment, outward growth occurs almost exclusively along the 18 edges of the hexagonal column. This is a diffusion-limited effect similar to the hollowing in Fig. 31. Then, rather suddenly, growth in the $\mathbb{T}$-direction takes over.

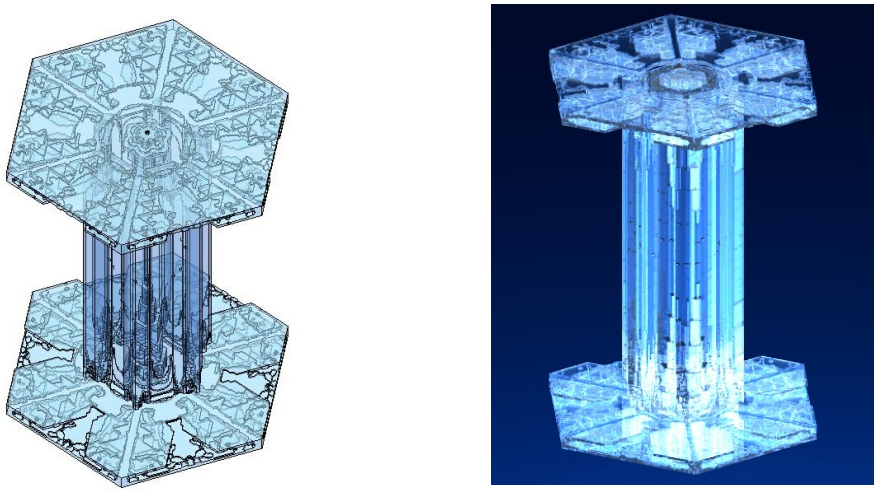

Fig. 37. A column capped with hexagonal plates.

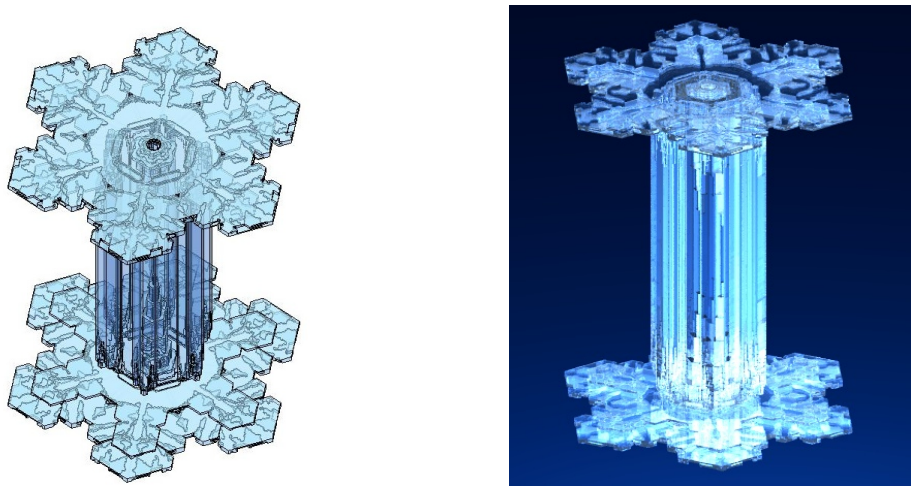

Fig. 38. A column capped with sectored plates.

13 Case study *vii* : eccentric crystals

This last section features snowfakes that result from a careful search through parameter space and are quite sensitive to any change. They are close-to-critical, near the phase boundary between dominant growth in the $\mathbb{Z}$-direction and the $\mathbb{T}$-direction. Consequently they may be rare in nature, though variants of some of the forms have been observed, and even represent morphological types in the Magono-Lee classification [**ML**]. All our final examples start from the canonical seed.

As mentioned in Section 2, starting from a single cell our algorithm has a strong tendency to grow rapidly in the $\mathbb{Z}$-direction due to the immediate onset of a *needle instability*. Even if the initial mesoscopic prism is wider in the $\mathbb{T}$-direction, it is still quite common for this instability to arise later on if the dynamics are close to critical. After an initial phase of typical planar growth, needles suddenly nucleate at concentric locations scattered over the central plate or arms. Fig. 137 of [**Nak**] shows an excellent example of this type in nature, and our first two examples illustrate a similar phenomenon in our model. The conventional explanation for such hybrid types, called *stellar crystals with needles* in [**ML**], involves a sudden change in the environment, but this is one of several cases where our algorithm suggests that homogeneous conditions can sometimes produce the same effect.

Fig. 39 has features like a classic planar snowflake that has developed *rime* from attachment of surrounding water droplets. In fact these protrusions are potential needle instabilities — the two symmetric rings close to the center and the tips are stunted needles, whereas the intermediate needles have successfully nucleated. The parameters of this snowfake are: $\beta_{01} = 1.58$, $\beta_{10} = \beta_{20} = \beta_{11} = 1.5$, $\beta_{30} = \beta_{21} = \beta_{31} = 1$, $\kappa \equiv .1$, $\mu \equiv .006$, $\phi = 0$ and $\rho = .1$. Partial symmetry of bumps in many natural crystals, statistically unlikely to be the result of rime, often indicates vestiges of rims and ribs after sublimation, but can also be due to nascent needles, as in the middle specimen of Plate 116 in [**Nak**]. Since the locations where needles nucleate are quite sensitive to changes in parameters, residual randomness in the mesoscopic dynamics is apt to degrade the symmetry.

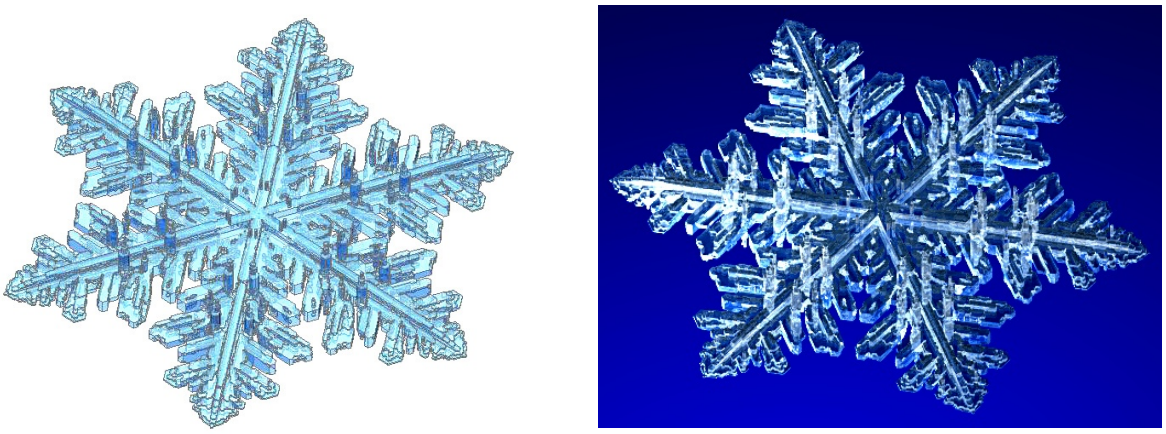

Fig. 39. A stellar dendrite with stunted and nucleating needles.

The next three examples have $\beta \equiv 1$, $\mu \equiv .03$, $\kappa_{10} = \kappa_{20} = .1$, $\kappa_{30} = .05$, and $\kappa_{11} = \kappa_{21} = \kappa_{31} = .01$. The remaining parameters for Fig. 40 are $\kappa_{01} = .11$ and $\rho = .06$. This snowfake is a rather extreme instance of a stellar crystal with needles in which the planar portion is a thick but very narrow simple star.

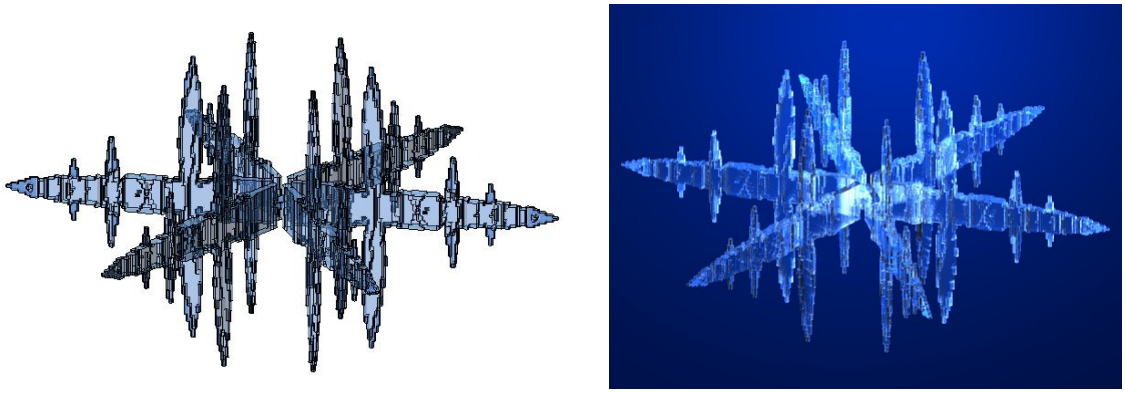

Fig. 40. A simple star with needles.

Our next two examples seem never to have been seen at all, and it is clear why: even if they managed to grow, their thin plates would be extremely brittle and susceptible to random fluctuations. They are characterized by very small differences in the growth rates. After starting as planar crystals, they suddenly nucleate thin structures extending into the third dimension. In Fig. 41 $\kappa_{01} = .12$ and $\rho = .057$; in Fig. 42 $\kappa_{01} = .116$ and $\rho = .06$. For obvious reasons, we call these *butterflakes*. They are idealizations of the *stellar crystals with spatial plates* in [**ML**]; chaotic snow crystals with thin plates growing every which way are relatively common.

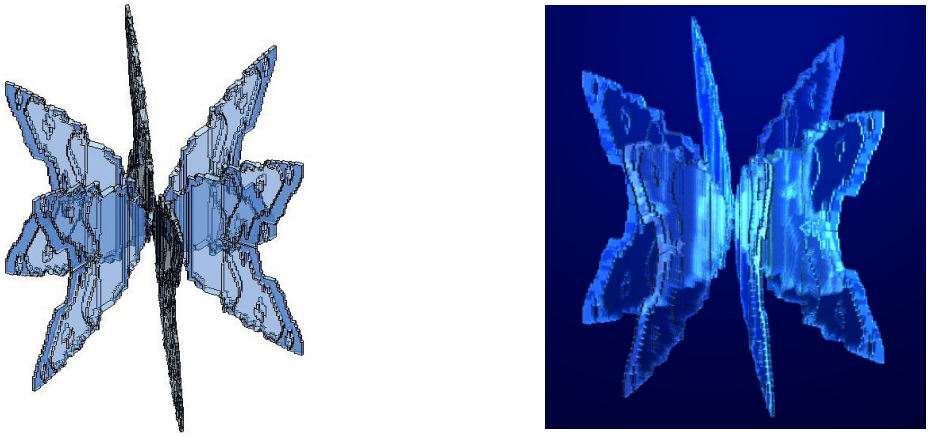

Fig. 41. A butterflake with wings in the directions of the main arms.

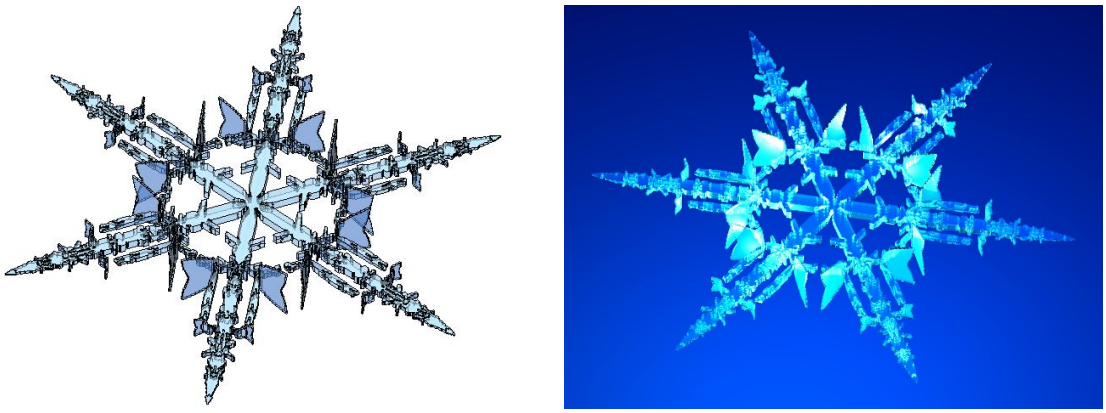

Fig. 42. A butterflake with side wings.

We conclude the paper with a family of five related examples. The first is a common sandwich plate (cf. p. 44, lower right, in [**Lib6**]) with parameter values $\beta_{01} = 1.41$, $\beta_{10} = \beta_{20} = 1.2$ $\beta_{11} = \beta_{30} = \beta_{21} = \beta_{31} = 1$, $\kappa \equiv .1$, $\mu \equiv .025$, $\phi = 0$, and $\rho = .09$.

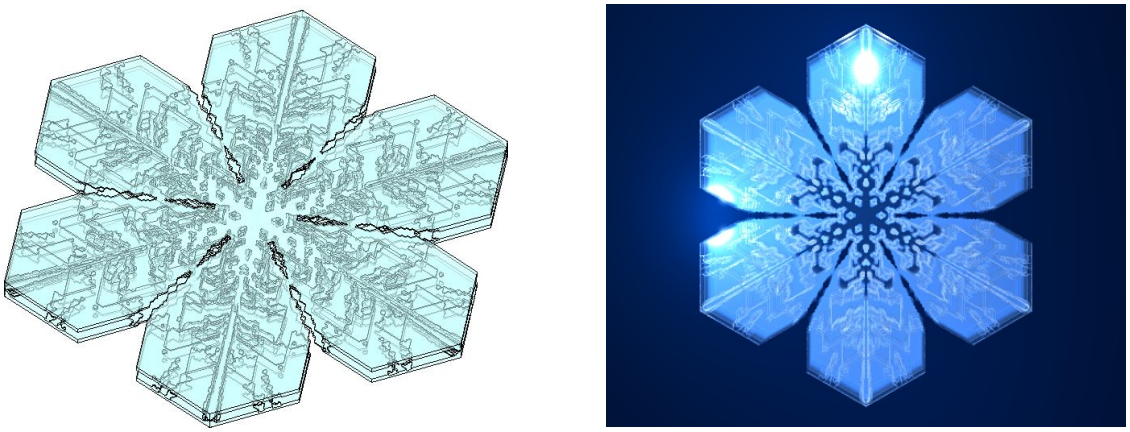

Fig. 43. A sandwich plate with broad branches.

The remaining four are minor perturbations, which nevertheless look quite different. Namely, even though their model parameters are constant over time, they undergo "exploding tips" quite similar to crystals such as the one in Fig. 35 that results from inhomogeneous environmental conditions. The principle behind all four variants is the same: eventually, the growing tip thickens and slows down considerably. Usually this happens close to the beginning of the evolution (as, in fact, occurred in the dynamics leading to Fig. 43), so the snowfake is unremarkable. But with some experimentation we find cases when the onset of the sandwich instability is delayed and the final picture can be quite dramatic. The complex inner patterns are the result of extraordinarily intricate dynamics. Parameter values that differ from those of Fig. 43 are given in the captions.

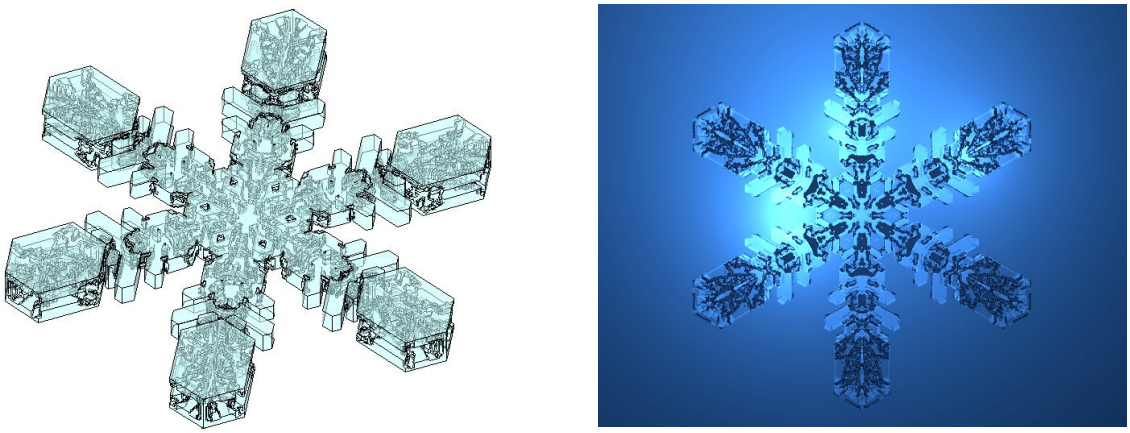

Fig. 44. Perturbed parameters: $\beta_{01} = 1.25$, $\rho = .091$.

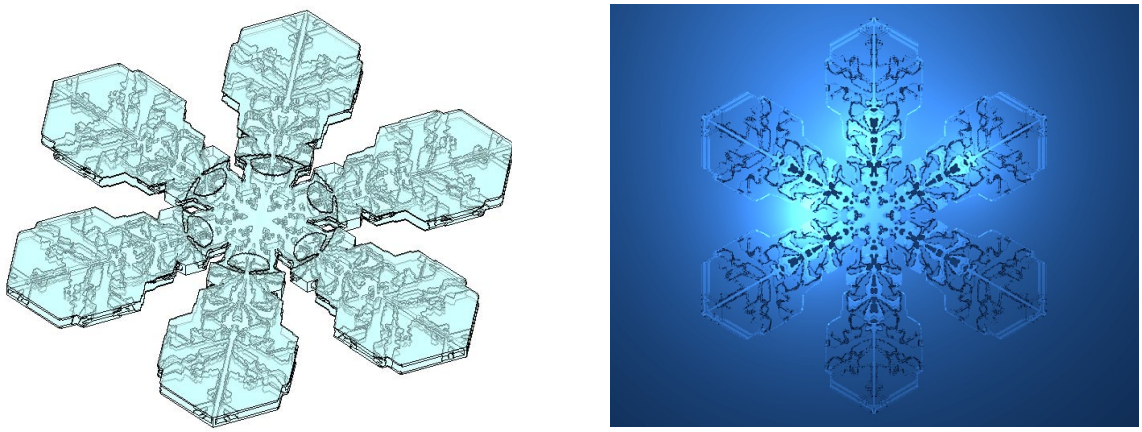

Fig. 45. Perturbed parameter: $\beta_{01} = 1.5$.

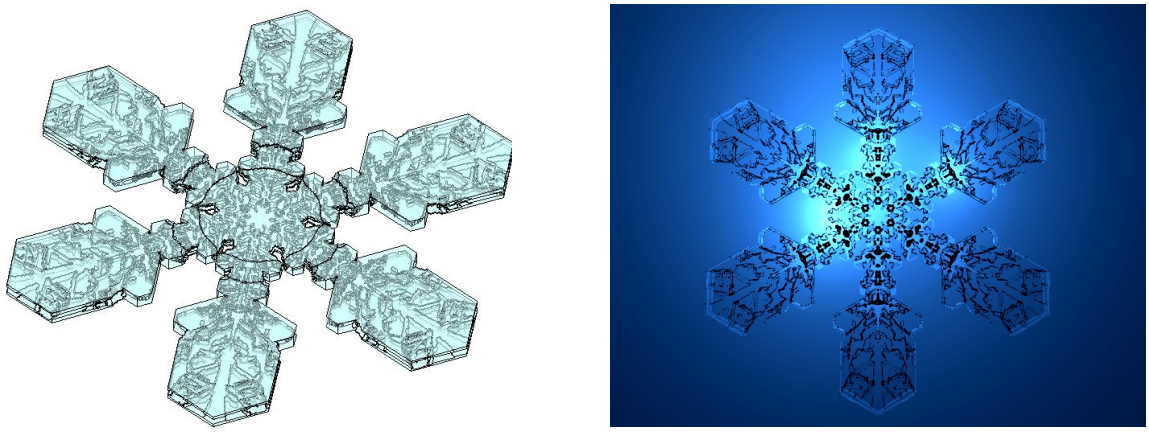

Fig. 46. Perturbed parameter: $\beta_{01} = 1.19$.

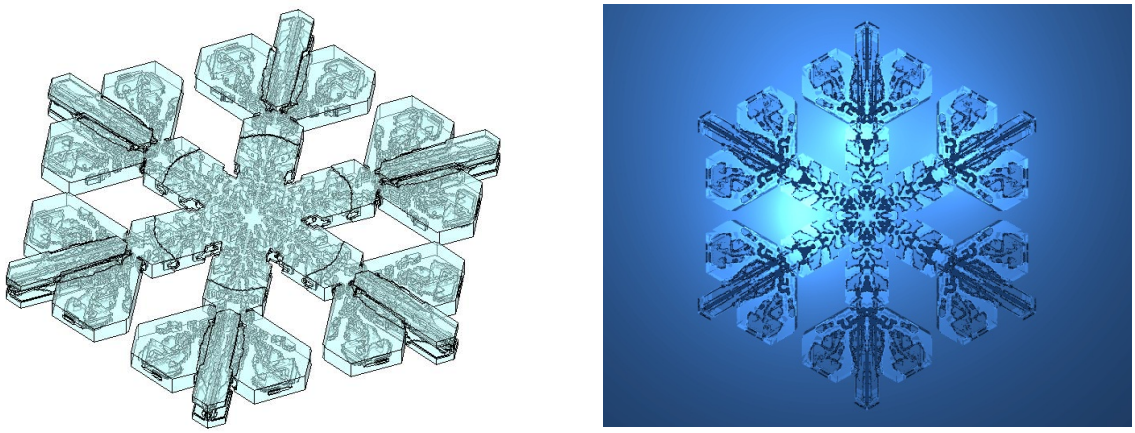

Fig. 47. Perturbed parameter: $\beta_{01} = 1.25$.

14 Summary and conclusions

We have presented a simple model of snow crystal growth that is based on a few physically reasonable assumptions: a strong convexifying force up to μm size, diffusion of water molecules off the crystal, exchange between attached and unattached molecules at the boundary, and non-isotropic attachment rates that favor concave parts of the boundary over convex ones. The variety of observed phenomena we are able to replicate strongly suggests that these are the most important ingredients for the formation of physical snow crystals. Below we list further conclusions from our experiments. We are confident they hold valid for our mathematical model, but it remains to be seen to what extent they can be verified in the lab or in nature.

- In predominantly two-dimensional crystals, the velocity of expansion in the prism direction does not need to be much larger than the one in the basal direction. In Section 8, for example, this difference is less than 7%.
- The range of motion of a snow crystal has to be quite limited during most of its growth, on the order of its final size. This motion is roughly equivalent to a small drift of water vapor, which can affect the distribution of markings on the basal facets of the crystal but otherwise has a limited effect on morphology. However, drift, along with early random fluctuations, appears to play an important role in the evolution of double plates in the case where one of them is stunted.
- Many, perhaps the majority of simple snow crystals are sandwich plates: two thin plates with ridges, ribs and other markings between them. These are the result of a newly identified sandwich instability that can occur either early in the evolution, or after the crystal has reached a sizable diameter, perhaps even 100μm or more. The latter scenario may create the illusion of a sudden change in vapor density, temperature, or pressure. The sole surface markings of sandwich plates are circular reverse shapes resulting from nucleation near the tips.

- Markings do appear on the surface (rather than between sandwich plates) of predominantly planar snowfakes for a very narrow range of parameters, suggesting that the most attractive snow crystals occur near a phase boundary. We are nevertheless able to replicate commonly observed phenomena such as ridges, flumes, and side branches with and without markings.
- Changes in environmental conditions do result in changes in morphology. These correspond well to experimental results for synthetic snow crystals [**Lib5**].
- In dendritic crystals, lower vapor density first leads to lower frequency of side branches, then to sandwich instabilities and relatively thick plates.
- The melting rate regulates the ability of attached molecules at the boundary to detach. Increasing this rate is another mechanism to reduce side-branching, arguably more important than reduced density.
- Three dimensional structures such as needles and columns are generically hollow, and form easily when growth in the basal direction is much preferred. Prism faces of such crystals also become hollow as this preference is diminished.
- Very interesting and completely new phenomena occur in our snowfake experiments when the preference for growth in the prism direction is only slight. These include the needle instability (nucleation of thin needles that grow in the basal direction), butterflake instability (thin plates that grow orthogonally to the main plane of growth), and exploding tips (dramatic widening of a star-like crystal's tips). Evidence for physical relevance of such eccentric dynamics is inconclusive.

References

[**BH**] W. A. Bentley and W. J. Humphreys, "Snow Crystals," McGraw-Hill, 1931 and Dover, 1962.

[**CK**] S. Choi, I. C. Kim, *Waiting time phenomena for Hele-Shaw and Stefan problems*, Indiana Univ. Math Journal (2006), 525–552.

[**EMP**] E. Erbe, C. Murphy, C. Pooley, *Electron Microscopy Unit Snow Page*. `http://emu.arsusda.gov/snowsite/default.html`

[**FT**] N. Fukuta, T. Takahashi, *The growth of atmospheric ice crystals: A summary of findings in vertical supercooled cloud tunnel studies*, Journal of the Atmospheric Sciences 56 (1999), 1963–1979.

[**GG1**] J. Gravner, D. Griffeath, *Random growth models with polygonal shapes*, Annals of Probability 34 (2006), 181–218.

[**GG2**] J. Gravner, D. Griffeath, *Modeling snow crystal growth I: Rigorous results for Packard's digital snowflakes*, Experimental Mathematics 15 (2006), 421–443.

[**GG3**] J. Gravner, D. Griffeath, *Modeling snow crystal growth II: A mesoscopic lattice map with plausible dynamics*, Physica D 237 (2008), 385–404.

[**GN**] T. Gonda and S. Nakahara, *Dendritic ice crystals with faceted tip growing from the vapor phase*, Journal of Crystal Growth 173 (1997), 189–193.

[**Iwa**] K. Iwai, *Three-dimensional structure of plate-like snow crystals*, J. Meteor. Soc. Japan 61 (1983), 746–755.

[**Kim**] I. C. Kim, *Uniqueness and Existence of Hele-Shaw and Stefan problem*, Arch. Rat. Mech. Anal. 168 (2003), 299–328.

[**Lib1**] K. Libbrecht, *Morphogenesis on ice: The physics of snow crystals*, Engineering and Science 1 (2001), 10–19.

[**Lib2**] K. Libbrecht, *Growth rates of the principal facets of ice between -10 C and -40 C,* Journal of Crystal Growth 247 (2003), 530–540.

[**Lib3**] K. Libbrecht, *Explaining the formation of thin ice crystal plates with structure-dependent attachment kinetics,* Journal of Crystal Growth 258 (2003), 168–175.

[**Lib4**] K. Libbrecht, *The physics of snow crystals*, Reports on Progress in Physics 65 (2005), 855–895.

[**Lib5**] K. Libbrecht, `http://www.its.caltech.edu/~atomic/snowcrystals/`

[**Lib6**] K. Libbrecht, "Field Guide to Snowflakes," Voyageur Press, 2006.

[**LR**] K. Libbrecht, P. Rasmussen, "The Snowflake: Winter's Secret Beauty." Voyageur Press, 2003.

[**ML**] C. Magano and C. Lee, *Meteorological classification of natural snow crystal*, J. Fac. Sci. Hokkaido 2 (1966), 321–335.

[**Nak**] U. Nakaya, "Snow Crystals: Natural and Artificial," Harvard University Press, 1954.

[**NB**] J. T. Nelson, M. B. Baker, *New theoretical framework for studies of vapor growth and sublimation of small ice crystals in the atmosphere*, J. of Geophys. Research 101 (1996), 7033–7047.

[**Nel**] J. Nelson, *Branch growth and side branching in snow crystals*, Crystal Growth & Design 5 (2005), 1509–1525.

[**NK**] J. Nelson, C. A. J. Knight, *Snow crystal habit changes explained by layer nucleation*, Journal of Atmospheric Sciences 55 (1998), 1452–1465.

[**NR**] C. Ning, C. Reiter, *A cellular model for 3-dimensional snow crystallization*, Computers & Graphics 31 (2007), 668–677.

[**Pac**] N. H. Packard, *Lattice models for solidification and aggregation*, Institute for Advanced Study preprint, 1984. Reprinted in "Theory and Application of Cellular Automata," S. Wolfram, editor, World Scientific, 1986, pp. 305–310.

[**POV**] *Persistence of Vision Raytracer*, Version 3.6 (2004).
`http://www.povray.org`

[**Rei**] C. Reiter, *A local cellular model for snow crystal growth*, Chaos, Solitons & Fractals 23 (2005), 1111–1119.

[**SB**] B. Shraiman, D. Bensimon, *Singularities in nonlocal interface dynamics*, Phys. Rev. A 30 (1984), 2840–2842.

[**Sch**] A. Schmidt, *Approximation of crystalline dendrite growth in two space dimensions*, Acta Math. Univ. Comenianae 67 (1998), 57–68.

[**TEWF**] T. Takahashi, T. Endoh, G. Wakahama, N. Fukuta, *Vapor diffusional growth of free-falling snow crystals between* $-3°$C *and* $-23°$C, J. Meteor. Soc. Japan 69 (1991), 15–30.